IMAGING TECHNIQUES FOR THE STUDY OF FOOD MICROSTRUCTURE: A REVIEW

PASQUALE M. FALCONE,* ANTONIETTA BAIANO,* AMALIA CONTE,* LUCIA MANCINI,† GIULIANA TROMBA,† FRANCO ZANINI,† AND MATTEO A. DEL NOBILE*

*Department of Food Science, University of Foggia
Foggia, FG 71100, Italy
†Sincrotrone Trieste S.C.p.A. in Area Science Park I
Basovizza, TS 34012, Italy

ADVANCES IN FOOD AND NUTRITION RESEARCH VOL 51 ISSN: 1043-4526

DOI: 10.1016/S1043-4526(06)51004-6

ABBREVIATIONS

S_v	Number of solid voxels. It corresponds to the solid phase (crumb) within the 3D testing sphere used in the stereological calculus.
V_v	Number of void voxels. It corresponds to the void phase (air) within the 3D testing sphere.
T_v	Total number of voxels. It is calculated by summing S_v and V_v.
δ	Crumb density (solid volume fraction). It was calculated as a ratio between S_v and T_v.
P	Crumb porosity (void volume fraction).
W_N	Cell wall number.
W_Th	Cell wall thickness.
W_Sp	Cell wall spacing.
SS	Specific surface. It is the solid phase surface per unit of crumb volume.
$\text{PrinMIL}_{1,2,3}$	Are the magnitude of the principal mean intercept length vectors (MILv) along the three main eigenvectors ($\vec{e}_1, \vec{e}_2, \vec{e}_3$). This parameter is related to the amount of solid phase along the main orientations of the cell structure cell walls.
Is_Ix	Is the isotropic index according to Falcone *et al.* (2004b), Benn (1994) and Ryan and Ketcham (2002). This parameter indicates the degree of difference of the MILv ellipsoid from the spherical shape and it is related to the degree of randomization of the solid phase around the primary orientation of the cell walls ($\vec{e}_1$).
El_Ix	Is the elongation index according to Falcone *et al.* (2004b), Benn (1994) and Ryan and Ketcham (2002). This parameter indicates the degree of elongation of the MILv ellipsoid and it is related to the solid phase spread around the tertiary orientations of the cell walls, ($\vec{e}_3$).
DA	Is the degree of anisotropy according to Falcone *et al.*, (2004b), Lim and Barigou (2004), Benn (1994), and Ryan and Ketcham (2002). This parameter corresponds to the inverse of the isotropic index and indicates the flatting degree of the MIL ellipsoid along the secondary favorite orientation of cell walls ($\vec{e}_2$).
$\text{DA}_{1,2,3}$	Are the relative degrees of anisotropy (Falcone *et al.*, 2004b). This parameter indicates the mean spread degree of the solid phase along the primary (1), secondary (2),

and tertiary (3) favorite orientation of the cell walls ($\vec{e}_1$, $\vec{e}_2$, $\vec{e}_3$).

FA Is the fractional anisotropy according to Matusani (2003). It is a complex index of anisotropy and takes into account both the isotropic index and the elongation index of the structure.

I. INTRODUCTION

A. IMPORTANCE OF MICROSTRUCTURE STUDIES

Quality of a food product is related to its sensorial (shape, size, color) and mechanical (texture) characteristics. These features are strongly affected by the food structural organization (Stanley, 1987) that, according to Fardet *et al.* (1998), can be studied at molecular, microscopic, and macroscopic levels. In particular, microstructure and interactions of components, such as protein, starch, and fat, determine the texture of a food that could be defined as the "external manifestation of this structure" (Allan-Wojtas *et al.*, 2001).

Concerning bread, characteristics such as cell wall thickness, cell size, and uniformity of cell size affect the texture of bread crumb (Kamman, 1970) and also the appearance, taste perception, and stability of the final product (Autio and Laurikainen, 1997). Crumb elasticity can be predicted from its specific volume and is strongly affected by the amylose-rich regions joining partially gelatinized starch granules in the crumb cell walls (Scanlon and Liu, 2003).

The structural organization of the components of a cheese, especially the protein network, affect the cheese texture; in particular the stress at fracture, the modulus, and work at fracture could be predicted very well from the size of the protein aggregates (Wium *et al.*, 2003). Cheeses having a regular and close protein matrix with small and uniform (in size and shape) fat globules show a more elastic behavior than cheeses with open structure and numerous and irregular cavities (Buffa *et al.*, 2001).

The mechanical properties of cocoa butter are strongly dependent on its morphology at microscopic level and, in particular, on the polymorphic transformation of the fat crystals and the coexistence of different polymorphic forms (Brunello *et al.*, 2003). Thorvaldsson *et al.* (1999) studied the influence of heating rate on rheology and structure of heat-treated pasta dough. They found that the fast-heated samples had pores smaller than the slow-heated ones and that the pore dimensions affect the energy required to cause a fracture. In particular, the energy required to determine a fracture in the samples having the smallest pores was more than that for the samples having the highest pores.

A study carried out on the effects of grind size on peanut butter texture demonstrated that an increase of that variable decreased sensory smoothness, spreadability, and adhesiveness (Crippen *et al.*, 1989).

Langton *et al.* (1996) studied correlations existing between microstructure and texture of a particulate proteic gel (spherical particles joined together to form strands). They found that the texture, as measured with destructive methods, was sensitive to pore size and particle size, whereas it was sensitive to the strand characteristics if measured with nondestructive methods.

Martens and Thybo (2000) investigated the relationships among microstructure and quality attributes of potatoes. They found that volume fractions of raw starch, gelatinized starch, and dry matter were positively correlated to reflection, graininess, mealiness, adhesiveness, and chewiness and negatively correlated to moistness.

From the evidence that microstructure affects food sensorial properties, an important consideration derives: foods having a similar microstructure also have a similar behavior (Kaláb *et al.*, 1995). Since microstructure is determined both by nature and by processing, food processing can be considered as the way for obtaining the desired microstructure (and consequently the desired properties) from the available food components (Aguilera, 2000). As a consequence, knowledge of microstructure must precede the regulation of texture (Ding and Gunasekaran, 1998) and other food attributes.

B. SUITABLE TECHNIQUES FOR MICROSTRUCTURE STUDIES

Studies on food structure at a microscopic level can be performed by using a large variety of microscopic techniques including light microscopy (LM), scanning electron microscopy (SEM), transmission electron microscopy (TEM), and confocal laser scanning microscopy (CLSM). Although magnification of LM is modest if compared to electron microscopy techniques, LM allows the specific staining of the different chemical components of a food (proteins, fat droplets, and so on). For this reason, it represents a technique suitable for the investigation of multicomponent or multiphase foods such as cereal-based foods (Autio and Salmenkallio-Marttila, 2001). LM, SEM, and TEM can be used to put in evidence different aspects of particulate structures. For example, in a study on microporous, particulate gels (Langton *et al.*, 1996), LM was used to visualize pores, TEM was applied to evaluate particle size, and SEM allowed to detect how the particles were linked together, that is, the three-dimensional (3D) structure. SEM and TEM allow a higher resolution if compared to LM but, as the latter, require sample preparation procedures (freezing, dehydration, and so on) that may lead to artifacts (Kaláb, 1984). CLSM represents a suitable alternative method in food microstructure evaluation because it require a

minimum sample preparation. In fact, the CLSM technique includes the optical slicing of the sample (Autio and Laurikainen, 1997; Rao *et al.*, 1992). CLSM can be used for examining the 3D structure of the protein network of pasta samples (Fardet *et al.*, 1998), doughs (Thorvaldsson *et al.*, 1999), or high-fat foods (Wendin *et al.*, 2000) that cannot be prepared for conventional microscopy without the loss of fat (Autio and Laurikainen, 1997).

The microstructure of bread and other microporous foods can be conveniently studied by applying synchrotron radiation X-ray microtomography (X-MT) (Falcone *et al.*, 2004a; Maire *et al.*, 2003) to centimeter- or millimeter-sized samples (Lim and Barigou, 2004). X-MT application only requires the presence of areas of morphological or mass density heterogeneity in the sample materials. The use of this technique for food microstructure detection is of recent date. It was traditionally used for the analysis of bone quality (Peyrin *et al.*, 1998, 2000; Ritman *et al.*, 2002).

Among the imaging techniques, atomic force microscopy (AFM) and magnetic resonance imaging (MRI) have been introduced into food science as nondestructive techniques. The first one is particularly suitable for studying surface roughness, especially in fresh foods (Kaláb *et al.*, 1995). The second one can be successfully applied for studying processing such as frying, foam drainage, fat crystallization, and other operations in which a dynamic study of food structure is needed (Kaláb *et al.*, 1995). Examples of MRI application are the researches of Takano *et al.* (2002) and Grenier *et al.* (2003) that qualitatively and quantitatively studied the local porosity in dough during proving, a stage in which invasive analytical methods may cause the dough collapse. MRI is based on the nuclear magnetic resonance (NMR) technique that has recently been introduced in investigations of dough and bread. It allows the study of the changes in distribution and mobility of different types of protons (fat, structural and bulk water) in a sample and, thanks to the high correlations between texture parameters and NMR relaxation data, NMR is suitable to predict firmness and elasticity of these foods (Engelsen *et al.*, 2001).

Ultrasound represents another promising technique able to investigate some structural properties of foods. Since the agreement between rheological (storage and loss moduli) and ultrasound measurements (velocity of ultrasound propagation and attenuation), ultrasound could be used as on-line quality control technique for dough (Ross *et al.*, 2004). Ultrasound can also be used to distinguish crystalline fats from liquid fats (McClements and Povey, 1988) or to determine a food composition (Chanamai and McClements, 1999). In fact, the speed of sound decreases with temperature in fat whereas increases with temperature in aqueous solutions (Coupland, 2004).

Information about the crystallinity level and crystal size in a food can be obtained by submitting the food matrix to X-ray diffraction. For example,

this technique supplies useful information about crystalline and gelatinized starch (Severini *et al.*, 2004).

Fourier transform infrared microspectroscopy (FTIR) and Raman microspectroscopy provide quantitative information about the chemical microstructure of heterogeneous solid foods (Cremer and Kaletunç, 2003; Piot *et al.*, 2000; Thygesen *et al.*, 2003) without sample destruction.

Another interesting technique able to investigate the microstructure of dense microemulsions is represented by the small-angle neutron scattering (SANS) (de Campo *et al.*, 2004).

Since many food characteristics are strongly dependent on microstructure, it is possible to obtain microstructural information by studying mechanical and viscoelastic properties of foods. A food sample submitted to mechanical tests gives rise to a force–time curve from which several parameters related to microstructure can be extrapolated: hardness, cohesiveness, springiness, chewiness, gumminess, stickiness (Martinez *et al.*, 2004). When submitted to a stress (under compression, tension, or shear conditions), food samples suffer a strain. The elastic modulus or Young's modulus of the analyzed sample can be obtained from the stress–strain curve (Del Nobile *et al.*, 2003; Liu *et al.*, 2003). The viscoelastic properties of a food can be expressed in terms of G', G'', and tan δ parameters. G' takes into account the elastic (solid-like) behavior of a material, G'' is a measure of the viscous (fluid-like) behavior of a material, and tan δ represents the ratio between G'' and G'. These parameters can be evaluated by performing dynamic mechanical and rheological tests (Brunello *et al.*, 2003; Kokelaar *et al.*, 1996; Ross *et al.*, 2004; Wildmoser *et al.*, 2004).

C. WHY IMAGING TECHNIQUES FOR MICROSTRUCTURE STUDIES?

Since sensory and mechanical properties of a food depend on its microstructure, the knowledge of microstructure must precede any operation aimed to the attainment of a specific texture (Ding and Gunasekaran, 1998). The instrumental measurements of mechanical and rheological properties represent the food responses to the forces acting on the food structure and, for this reason, are affected by the way in which these analyses are performed. Furthermore, mechanical and rheological tests are always destructive and make impossible the execution of other analyses.

As reported earlier, several types of microscopy techniques can be used for the observation of food microstructure. They allow the generation of data in the form of images (Kaláb *et al.*, 1995). Because of the artifacts due to the preparation of samples before microscopy analysis, it is advisable to apply a variety of techniques to the same samples in order to compare the

results obtained. Another limit of microscopic techniques is represented by the so-called "optical illusions," that is, the tendency of human eye to see what one is looking for (Aguilera and Stanley, 1999). This means that human eye is not suitable for objective evaluation.

The application of the traditional microscopic techniques is also affected by the difficulty of quantifying the structural features. Computer image analysis allows to process images in order to extract numerical data referred to the microstructure (Ding and Gunasekaran, 1998; Inoue, 1986; Kaláb *et al.*, 1995).

In the last years, the use of image analysis techniques has increased. Novaro *et al.* (2001) applied the image analysis to whole durum wheat grains in order to predict semolina yield. Quevedo *et al.* (2002) used the fractal image texture analysis to quantitatively analyze the surface of several foods (potato chips, chocolate, and so on) and to evaluate the potato starch gelatinization during frying and the chocolate blooming. Basset *et al.* (2000) and Li *et al.* (2001) applied the image texture analysis for the classification of meat.

Generally, microstructural features (<100 μm) obtained from digital images without any intrusion opened new opportunities in the field of the food evaluation. Several possibilities and instrumental facilities are available in order to acquire internal details at a microscopic level by means of optical, electronic, and more sophisticated systems. Furthermore, engineers try to develop physical models and numerical algorithms to determine accurate and quantitative information from digital images. At a first level of analysis there are several commercial softwares able to perform basic tasks such as image editing, segmentation, object selection, and measurement of global geometrical features such as volume fraction and specific surface area. A second level of analysis is performed by algorithms for the shape recognition and statistical classification of objects into specific classes.

With the rapid growth of computing and imaging tools, such as the X-ray–computed tomographic scanners, both 2D and 3D digital images of the internal structure can be readily acquired with high resolution and contrast and without any sample preparation. These images can be processed by means of the fractal and stereological analysis in order to quantify a number of *structural elements*. Fractal analysis allows to investigate the fractal geometry in both 2D and 3D digital images. Stereology, instead, allows to obtain 3D features from 2D images. These data-processing techniques represent new promising approaches to a full characterization of complex internal structures. Such advances in food evaluation open new horizons for the development of mathematical and computational models able to individuate the interactions between product microstructure and their mechanical properties.

D. STEPS OF THE IMAGE-PROCESSING ANALYSIS

Independently on the way of image acquisition, the image-processing analysis consists of the following five steps: image acquisition, preprocessing, segmentation, object measurement, and classification.

1. Image acquisition

Images are the spatial representations of objects (Gunasekaran, 1996). They are stored as matrixes of x columns by y rows containing thousands of cells called "pixels" (picture elements). Each pixel contains a numerical value (digital number) that represents the sensor reading (www.geog.ubc.ca/courses/geog470/notes/image_processing/). The image acquisition just consists in the capture of an image in this digital form. The prerequisite for the image quality is represented by lighting conditions during the image acquisition. Although there are a variety of image acquisition techniques (described in section II), a few types of devices are generally used for capturing images. They are represented by video cameras, scanners, magnetic resonance imagers, ultrasound scanners, and tomographs (Aguilera and Stanley, 1999).

2. Preprocessing

The aim of this operation is the improvement of the quality of an image, in order to remove distortions or enhances some image characteristics. Preprocessing includes pixel preprocessing and local preprocessing (Du and Sun, 2004).

a. Pixel preprocessing. Pixel preprocessing consists of a color space transformation. Color images are, in fact, normally acquired as 24 bit RGB (red, green, blue) images. But most programs are able to operate on gray scale (8 bit, monochrome), so the first step after acquisition consists in the transformation of the RGB digital color image in a gray scale image or in three monochrome images (monochrome red, monochrome green, and monochrome blue). Since 256 gray levels are available, each of the image pixels can have an integer value ranging from 0 (black) to 255 (white). In food image analysis, to better distinguish among the different parts of an object, it is preferable to transform the RGB color space in the HSI (hue, saturation, and intensity) channels (Li *et al.*, 2001; Sun and Brosnam, 2003; Tao *et al.*, 1995). Another color space is represented by the L*a*b* space that separates lightness (gray scale intensity) from two orthogonal color axes, a* that takes into account the content of red or green and b* that

considers the content of yellow and blue. HSL and HSV are two similar sets of coordinates that separate the gray scale brightness (L for luminance or V for value) from the hue (that is the distinction between red, orange, yellow, green, and so on) and from the saturation (the amount of color, e.g., the difference between pink and red).

b. Local preprocessing. Sometimes it is necessary to improve the image because of a nonuniform illumination or brightness across the image or the insufficient signal. These problems are generally solved using the so-called "point processes" that replace pixel values based on the individual values with new values based on the averaging brightness values of points having similar properties to the processed points. Different types of filters are used as a function of the noise magnitude (Goodrum and Elster, 1992; Leemans *et al.*, 1998; So and Wheaton, 1996; Utku and Koksel, 1998).

An alternative to filtering is represented by binarization that allows the transformation of the color or gray level image into a black-and-white image. In this way a value of black or white is assigned to each pixel (Aguilera and Stanley, 1999). After binarization, images can be manually edited so as to remove artifacts and noise and to apply other functions. The binary image is then ready for quantitative analysis performed by using stereological or morphometric methods.

3. *Segmentation*

It is the step that allows the separation of the image into features and background. Obviously, pixels contained in an object or features have values similar to those of the pixels belonging to the same category. Segmentation may be done manually or automatically.

Segmentation can be performed according to four different approaches: thresholding based, region based, gradient based, and classification based. In current applications, the first two methods are generally preferred (Du and Sun, 2004).

The thresholding-based segmentation is the simplest segmentation method but it works well if the objects have uniform gray level clearly distinguishable from the background that must have a different but uniform gray level with respect to the objects.

The region-based segmentation is a more powerful segmentation approach and includes two methods. The first, called "region growing and merging," acts by grouping pixels into larger regions as a function of homogeneity criteria. Successively, the second method, called "region splitting and merging," divides the image into smaller regions according to other criteria (Du and Sun, 2004).

The gradient-based segmentation, instead, allows to directly find the edges by their high-gradient magnitudes.

The classification-based method uses statistic or other techniques to assign each pixel to the different regions of the image.

4. Object measurement

After segmentation, it is possible to measure the features of interest for each of the individuated objects. The measurable features regard size (area, perimeter, length, width), shape (circularity, eccentricity, compactness, extent, and so on), color, and texture (smoothness, coarseness, graininess) (Du and Sun, 2004). Texture, in particular, is evaluated on the base of the gray level variation within the object (Aguilera and Stanley, 1999).

5. Classification

It allows to attribute a new object to one of the individuated categories by comparing the measured characteristics of the new object to those of a known one. Also in this case, several approaches are available: statistical, fuzzy, neural network.

The statistical classification uses probability models to classify objects.

The fuzzy classification method groups objects into categories without defined boundaries so as to take into account the degree of similarity of the considered object with respect to the others (Du and Sun, 2004).

Finally, the artificial neural network methods try to imitate human intelligence with the power of statistic.

II. IMAGE ACQUISITION TECHNIQUES

A. LIGHT MICROSCOPY

Microscopes used in LM are composed of a beam of visible light (photons) that represents the illumination source (probe), a system for focusing the source onto the sample (the condenser or condense glass lens), a location to place the sample or specimen, and the objective.

There are different types of LM: bright field (dark field viewing, phase contrast, oil immersion microscopy, differential interference contrast), polarizing, and fluorescence microscopy.

In the conventional bright field microscopy, light from an incandescent source is sequentially transmitted through the condenser, the specimen, an objective lens, and a second magnifying lens, the ocular or eyepiece, prior to reaching the eye. Some microscopes have an internal illuminator, while

others use a mirror to reflect light from an external source. If the specimen is not very colored, several mechanisms for the formation of contrast can be performed. For example, it is possible to use dyes or stains specific for the different components of the specimen (fast green and acid fuchsin for proteins, toluidine blue O for pectin and lignin in vegetables and for muscle and fibroblasts in meat, oil red O for fats) (Kaláb *et al.*, 1995).

Bright field microscopy is suitable to observe stained bacteria, thick tissue sections, thin sections with condensed chromosomes, large protists or metazoans, living protists or metazoans, algae, and other microscopic plant material.

Limitations of the bright field microscopy are little related to magnification, whereas they are highly dependent on resolution, illumination, and contrast. Resolution can be improved using oil immersion lenses, whereas lighting and contrast can be greatly improved using modifications of the technique such as dark field, phase contrast, oil immersion microscopy, differential interference contrast (DIC). Dark field viewing is obtained by placing an opaque disk in the light path between source and condenser so that only light that is scattered by particles on the slide can reach the eye. In this way, light does not pass through the specimen but is reflected by it. Sometimes, neither bright field nor dark field can be used: the first due to the little contrast between the structures belonging to the same object, the second due the too thin section of the samples. In these cases, the phase contrast microscopy is applied by exploiting the differences in the refractive index of the various parts of the object. Oil immersion microscopy is an interesting alternative to bright field. In fact, when light passes from a material having a refractive index to a material having another refractive index, light bends and causes a loss in resolution, in particular at high magnifications. It is possible to improve resolution by placing a drop of oil with the same refractive index as glass between the cover slip and objective lens so as to eliminate two refractive surfaces (www.ruf.rice.edu/~bioslabs/methods/microscopy/microscopy.html). In DIC microscopy, a minute difference in refractive indexes of light passing through an unstained specimen is transformed into a monochromatic shadow-cast image so as to allow the observation of living and thick specimens (www.nikon-instruments.jp/eng/tech/1-0-4.aspx).

An alternative to the bright field microscopy is represented by the polarizing microscopy obtained by inserting two polarizers in the light path, the first between light source and specimen and the second between the objective and the eye. The light produced by the first polarizer vibrates in one of the planes perpendicular to the direction of travel. By opportunely rotating the second polarizer (called analyzer), it is possible to distinguish within a specimen the amorphous region (that appears dark) from the crystalline domains (that appears bright because of their birefringence).

In fluorescence microscopy, specimen itself represents the light source. This method is based on the phenomenon that certain material can absorb light of a specific wavelength and emit energy detectable as light of a longer wavelength and lower intensity. The sample can either be fluorescing in its natural form (autoflorescence) or treated with fluorescing chemicals. In vegetable tissues, autofluorescent molecules are, for example, chlorophyll, carotenoids, lignin, and ferulic acid. In animal tissues, the main sources of fluorescence are some fats.

B. CONFOCAL LASER SCANNING MICROSCOPY

CLSM allows the observation of thin optical sections in thick, intact specimens. CLSM represents an advanced technology with respect to fluorescence microscopy. In fact, in conventional fluorescence microscopy, out-of-focus fluorescence can cover the image details. Instead, to induce fluorescence, CLSM uses a laser spot that is scanned in lines across the field of view resembling image formation by an electron beam in a computer screen. In this way, sample is illuminated and imaged one point at a time, whereas in the LM the object is uniformly illuminated. Fluorescence is detected by a highly sensitive photomultiplier. Out-of-focus fluorescence is excluded by the presence of a pinhole at the focal plane of the image able to produce a sufficiently thin laser beam (Kaláb *et al.*, 1995). Resolution increases as the open degree of the confocal pinhole decreases. Furthermore, the intensity of the laser beam decreases with the third potency above and below the focal plane (www.plbio.kvl.dk/~als/confocal.htm). Also, in CLSM it is possible to use fluorescent labels to put in evidence specific food components. CLSM allows the extraction of topographic information from a set of confocal images acquired over a number of focal planes. Multiple confocal slices of the image can be obtained. In this way, a 3D topographic map of the object is available (Ding and Gunasekaran, 1998).

Light microscopes are limited by the physics of light to 500x or 1000x magnification and a resolution of 0.2 μm. The image resolution is related to the beam wavelength that in the case of LM and CLSM ranges from 400 to 600 nm, whereas in the case of electron microscopy is of 0.0037 nm (Hermansson *et al.*, 2000). The very short wavelength of electrons allows the resolution improvement and modern technology makes it easy to obtain a resolution of 3 nm or lower (www.hei.org/research/depts/aemi/emt.htm).

C. ELECTRON MICROSCOPY

It allows the obtainment of information about topography (surface features of an object, i.e., its texture and relation among these features and the material properties), morphology (shape and size of the particles and relation among

these structures and the materials properties), and composition (elements, compounds, and their relative amounts, relationship between composition and materials properties).

Since in electron microscopy the illumination source is represented not by light but by a focused beam of electrons, the resulting micrographs cannot be in color but in various shades of gray. Colors can be successively added to the obtained micrographs. Individual components can be distinguished thanks to the differences in their affinity for various heavy metals such as osmium, ruthenium, lead, and uranium. Gold granules of dimensions of few nanometers attached to antibodies may be used to identify macromolecules (enzymes, protein-based hormones, and so on) through immunological reactions.

In an electron microscope, a stream of electrons is formed by the electron source and is accelerated toward the specimen using a positive electric potential. The stream is focused into a thin, monochromatic beam by using metal apertures and magnetic lenses. The electron beam interacts with the specimen and the effects of these interactions are detected and transformed into an image.

Electron microscopy works under vacuum conditions because air absorbs electrons. For these reasons, wet samples cannot be analyzed by electron microscopy without previous dehydration, freezing, or freeze-drying due to the sublimation phenomena (Bache and Donald, 1998).

Electron microscopy can be divided into SEM and TEM. These two types of electron microscopy differ from each other in the way in which the image is formed. The transmission electron microscope was the first type of electron microscope to be developed (1931) and it works exactly as a light transmission microscope except for the focused beam of electrons used in place of light. The first scanning electron microscope was built in 1942 but was commercially available in 1965 due to the complicated electronics involved in "scanning" the beam of electrons across the sample.

1. Transmission electron microscopy

It allows to determine the internal structure of materials. The structure of a transmission electron microscope constitutes of an evacuated metal column with the source of illumination, a tungsten filament (the cathode), at the top. When the filament is heated at a high voltage, the filament emits electrons. These electrons are accelerated to an anode (positive charge) and pass through a tiny hole in it to form an electron beam that passes down the column. Electromagnets placed in the column work as magnetic lens. The electron beam is focused onto the specimen. Some electrons pass through the sample and the image, magnified by the intermediate lens, is observed, thanks to the projector lens, on a fluorescent screen at the base of the microscope column or

photographed (www.hei.org/research/depts/aemi/emt.htm). The image formation is due to the differences in electron density of the analyzed samples or due to the thickness of the metal replica (Kaláb *et al.*, 1995).

To allow electrons to transmit through the materials, samples have to be very thin (50–100 nm). The energy of the electrons in the TEM determines the relative degree of penetration of electrons in a specific sample. So energy of 400 kV provides high resolution and high penetration in samples of medium thickness. TEM resolution often exceeds 0.3 nm (Yada *et al.*, 1995). TEM allows to obtain magnifications of 350,000 times and over (www.uq.edu.au/nanoworld/tem_gen.html).

In TEM, thin sections of samples are embedded in epoxy resins or, alternatively, platinum-carbon replicas of the samples are produced in order to the avoid release of vapor or gases.

Contrast in the TEM increases as the atomic number of the atoms in the specimen increases. Since biological molecules are composed of atoms of very low atomic number (carbon, hydrogen, nitrogen, and so on), contrast is increased with a selective staining, obtained by exposure of the specimen to salts of heavy metals, such as uranium, lead, and osmium, which are electron opaque (www.hei.org/research/depts/aemi/emt.htm).

2. *Scanning electron microscopy*

It allows the detection of the sample surface that emits or reflects the electron beam (Hermansson *et al.*, 2000). To provide electron conductivity, a 5- to 20-nm coating is applied on the sample surface (Kaláb *et al.*, 1995).

In conventional SEM to avoid the vapor release samples are previously dried, whereas in cryo-SEM samples are frozen and analyzed at low temperature.

Wet samples can be analyzed without a previous preparation by the so-called environmental scanning electron microscopy (ESEM). In this technique, instead of the vacuum conditions, the sample chamber is kept in a modest gas pressure (Bache and Donald, 1998). The upper part of the column (illumination source) is kept in high vacuum conditions. A system of differential pumps allows to create a pressure gradient through the column (Bache and Donald, 1998; Stokes and Donald, 2000). The choice of the gas depends on the kind of food: hydrated food is kept under water vapor.

D. MAGNETIC RESONANCE IMAGING

MRI is an analytical imaging technique primarily used in medical settings in order to produce high-quality images of the insides of the human body. Nevertheless, food applications of the MRI technique have been developed

in the last years. MRI is based on the principles of the NMR, a spectroscopic technique used by scientists to obtain chemical and physical information about molecules. It was named magnetic resonance imaging rather than nuclear magnetic resonance imaging (NMRI) because of the negative connotations associated with the term "nuclear" in the late 1970s. MRI started out as a tomography imaging technique, which allowed the conversion of the NMR signal deriving from a thin slice through the material in an image. This technique is based on the absorption and emission of energy in the radio frequency range of the electromagnetic spectrum (Bows *et al.*, 2001; Van Duynhoven *et al.*, 2003). Magnetic resonance images are based on proton density and proton relaxation dynamics, differing from those produced by using X-rays that are associated to the absorption of X-ray energy instead. The generation of magnetic resonance images can be controlled by the radio frequency pulse sequence used for exciting the nuclear spins. In the NMR, hydrogen nuclei are subjected to a strong magnetic field that determines their alignment in a spin-up or spin-down orientation. If a radio frequency pulse is applied to this system, the nucleus alignment is inverted and their individual processions will be brought into phase. When the radio frequency is switched off, the phase relationship decays with a characteristic time constant referred to as T2, and the nucleus alignment relaxes with a different time constant named T1. Both these parameters are temperature dependent. The chemical shift is another parameter that results from the electron clouds that shield each nucleus from the applied magnetic field, thus altering their frequency of NMR precession. A magnetic resonance image is composed of several picture elements called pixels. The intensity of a pixel is proportional to the NMR signal intensity of the contents of the corresponding volume element. The main advantage of the MRI technique is that it allows the obtainment of 2D or 3D images of the inner part of a material in a noninvasive and nondestructive way and without any preliminary sample preparation (Martinez *et al.*, 2003). MRI technique permits the spatial distribution of water, fat, and salt content in foods. In particular, its ability to study the spatial distribution and mobility of water and its dependence on temperature has led to a new approach to the validation of thermal processing in food manufacture. For example, Bows *et al.* (2001) used MRI to map the temperature distribution induced in water-based foods by microwave and conductive heating in order to evaluate their suitability as potential tools for microbiological assurance. NMR parameters, such as the relaxation times and diffusion coefficients, allow the definition of the interactions among water and other molecules. The attributes that can be quantified by applying MRI range from the composition of a material (moisture and fat content) to its physical (color, size, shape, volume) and chemical (density, viscosity, pH, water activity) properties. MRI can be used to control food processes and to

understand the changes occurring in food during processing. MRI not only permits the detection of internal defects of products, such as fruits and vegetables (hollow heart in potatoes, brown center and bruises in apples, freeze damage in oranges), but also more complex analysis regarding the grading of the quality of some foodstuffs. Internal structures, differentiated by water or fat content, can be highlighted by MRI because water, lipid, and proteins contain nuclei distinguishable by their NMR chemical shifts. The signals can be localized by the imposition of magnetic field gradients. The use of NMR microimaging to characterize water properties in cooked and high-pressure-treated beef as a function of the length of the ageing period was proposed by Bertram *et al.* (2004). Ishida *et al.* (2001) introduced the use of MRI to study the architecture of baked bread made of fresh or frozen dough. The NMR imaging represented an alternative to SEM technique to provide a quantitative estimation of the network structure of bread as one of the main elements determining the quality of the product. The method, providing information about the internal structure with a spatial resolution of 100 μm, was suitable for depicting crust surface and gluten network. The quality of frozen dough is generally lower than that of fresh dough because of the degradation of the gluten structure, the partial disruption of gluten fibrils, the separation of starch granules, and the deterioration of starch consequently to the ice crystal formation. The study of local porosity by means of the MRI gray level has been also presented and validated at whole dough scale by other authors (Grenier *et al.*, 2003). Bonny *et al.* (2004) used MRI to examine the dough fermentation process in terms of bubble size distribution and cell wall thickness. The classification of objects with different internal structure with respect to MR-image gray tone distribution has been used for the simple analysis of potato structure and texture (Thybo *et al.*, 2004). Another field of application of MRI technique is the visualization of lipid migration or oil distribution in food products. In a paper by Miquel *et al.* (2001), MRI was used to study the migration of hazelnut oil into chocolate in a composite confectionery. Yan *et al.* (1996) presented a work on the oil distribution in two types of crackers, laminated and non-laminated. NMR images represented the proton density map of the oil distribution. MRI has been successfully used to visualize the phase transition within food products during freezing. In this area, the mathematical models fail to give information on the variations of heat transfer that, instead, are detected by MRI from the differences in the product sugar concentration (McCarthy and McCarthy, 1996). Kerr *et al.* (1998) applied MRI technique to follow the ice formation in several foods during freezing. They used an image resolution of 350 μm, suitable for viewing macroscopic movement at the ice interface. Kuo *et al.* (2003) observed the ice formation during freezing of pasta filata and nonpasta filata mozzarella cheeses by mapping the

distribution of water through MRI. Renou *et al.* (2003) investigated the NMR parameters during freezing process of meat. A decrease of signal strength means a reduction of proton mobility during phase transitions. So the transition from water to ice can be inferred from a decrease in signal strength, whereas the time required for the disappearance of the NMR signal corresponds to that required for reaching a steady state enthalpy value. The major limitation of MRI is that it can be applied to material investigations only if they have a sufficient water content. Furthermore, the equipment required for MRI measurement is expensive.

E. ULTRASONIC IMAGING

The basis of the ultrasonic analysis of foods is the relationship between their ultrasonic properties (velocity, attenuation coefficient, and impedance) and their physical and microstructural properties (Coupland, 2004; Povey and McClements, 1988). Ultrasonic waves propagate more or less easily depending on material density and elastic modulus. Ultrasonic properties are also frequency dependent, particularly in the case of highly structured materials. The attenuation coefficient is a measure of the decrease in amplitude of an ultrasonic wave and it is expressed as the logarithm of the relative change in energy after traveling unit distance. It is a consequence of absorption and scattering. In the first case, the energy stored as ultrasound is converted into heat. In the second case, the energy is still stored as ultrasound but it is not detected because its propagation direction and phase have been altered. Like the ultrasonic velocity and attenuation coefficient, the acoustic impedance is a fundamental physical characteristic that depends on the composition and microstructure of a material so its measure can be used to provide valuable information about the properties of foods. The relationship between ultrasonic parameters and microstructural properties of a material can be empirically established by a calibration curve that relates the property of interest to the measured ultrasonic property or, theoretically, by using equations that describe the propagation of ultrasound through the material. Ultrasonic waves are similar to sound waves, but they have frequencies that are too high to be detected by the human ear. An ultrasonic wave is transmitted as a series of small deformations in the medium. When an oscillatory force is applied to the surface of the material, it is transmitted through it. If the force is perpendicularly applied, a compression wave is generated. Finally, if it is applied parallel to it, a shear wave is generated (Povey and McClements, 1988).

The key elements of an ultrasonic measurement system are: a transducer, which converts an electrical impulse into mechanical vibration, a signal generator to produce the original electrical excitation signal, and a display

system to record and measure the echo patterns produced. The pulser-receiver generates an electrical pulse that is sent to an ultrasonic transducer, where it is converted into an ultrasonic pulse that travels into the sample being analyzed. The signal received from the sample is converted back into an electrical pulse by the transducer and sent to the analog-to-digital converter where it is digitized. The two ways for characterizing the encompassment of these elements are the pulse-echo and the resonance techniques (Coupland, 2004). The first one is a useful way to measure the surface ultrasonic properties of a sample. Pulsed methods are commonly used as the basis for ultrasonic imaging devices.

By measuring distance, velocity, and attenuation as a function of the transducer position, it is possible to generate a 2D image of the sample properties. By rotating the sample, a 3D image can be reconstructed (Coupland, 2004).

Unlike light-scattering studies, for which dilution is often a prerequisite, ultrasound can measure food properties at concentrations that are technologically relevant. This aspect has obvious benefits for the analysis of inhomogeneous foods such as solidifying fats, dynamically changing dairy food systems, dough, and emulsions.

In the food industry, the applications of ultrasound can be divided into two distinct categories, depending on whether they use low-intensity or high-intensity ultrasound. The low-intensity ultrasound is a nondestructive tool because it uses power levels so small that no physical or chemical alterations in the material occur (Javanaud, 1998). In contrast, the power level used in the high-intensity ultrasound is so large that it causes physical disruption or promotes chemical reactions (McClements, 1995). The low-intensity ultrasound is commonly applied to provide information about properties of foods such as composition, structure, and physical state. Low-intensity ultrasound offers the possibility of acquiring images of the internal structure of foods for their quality evaluation. A small size ultrasonic probe (2 MHz) equipped with a LCD display was used for evaluating meat quality (Ozutsumi *et al.*, 1996). The picture signals were fed into a computer for the estimation of the fat content and other chemical characteristics of the meat. The results obtained were in agreement with the actual carcass measurements. An automatic classification equipment, based on the use of ultrasound imaging, was developed in order to measure the texture of cheese (Benedito *et al.*, 2000), correlate some meat textural features with the intramuscular fat content (Kim *et al.*, 1998), and measure fat and meat depth in carcasses (Busk *et al.*, 1999). Unlike meat classification systems, ultrasonic imaging is a noninvasive method for the on-line determination of lean meat percentage in carcasses and has low costs of maintenance. A novel approach to grading pork carcasses was proposed by Fortin *et al.* (2003). In this study,

ultrasound imaging was use to scan a cross-section of the loin muscle and capture 2D and 3D images of the carcasses. By coupling muscle area measures and fat thickness obtained by ultrasound together with 2D and 3D images, it was possible to provide the most accurate model for estimating salable meat yield. With respect to many others applications of ultrasound in food industry, ultrasonic inspection of meat quality has been developed to the stage of availability of commercial instruments. The use of ultrasound to measure muscle and fat depths for the initial screening of meat was proposed as an alternative method to X-ray computer tomography (CT) or MRI (Chi-Fishman *et al.*, 2004; Jones *et al.*, 2004). The CT measure of muscularity was positively associated with those performed by ultrasound. Compared with CT and MRI, ultrasound is a considerably less expensive and relatively more portable imaging technique. Ultrasound technology provides quantitative and qualitative information about mass features that may be linked to measures of muscles strength. There are two modes for ultrasonic imaging of biological tissue. One is the A-mode (amplitude modulation) and the other is the B-mode (brightness modulation). The first mode is one-dimensional and is used to measure depth of tissue, whereas the B-mode provides the characterization of biological tissue. Real-time ultrasound (RTU) technique is used as a special version of the B-mode technique in order to provide images of moving objects (Du and Sun, 2004).

An application of ultrasound that is becoming increasingly popular in the food industry is the determination of creaming and sedimentation profiles in emulsions and suspensions (Basaran *et al.*, 1998). Acoustic techniques can also assess nondestructively the texture of aerated food products such as crackers and wafers. Air cells, which are critical to consumer appreciation of baked product quality, are readily probed due to their inherent compressibility (Elmehdi *et al.*, 2003). Kulmyrzaev *et al.* (2000) developed an ultrasonic reflectance spectrometer to relate ultrasonic reflectance spectra to bubble characteristics of aerated foods. Experiments were carried out using foams with different bubble concentration and the results showed that ultrasonic reflectance spectrometry is sensitive to changes in bubble size and concentration of aerated foods.

Some of the simplest ultrasonic measurements involve the detection of the presence/absence of an object or its size from ultrasonic spectrum (Coupland and McClements, 2001). An ultrasonic wave incident on an ensemble of particles is scattered in an amount depending on size and concentration of the particles. As the ultrasonic parameters depend on the degree of the scattering, it can therefore be used to provide information about particle size.

Chow *et al.* (2004) reported dynamic video images of the influence of ultrasonic cavitation on the sonocrystallization of ice at a microscopic level. The ultrasonic device was used in combination both with an optical

microscope and with an imaging system in order to observe the production of secondary ice nuclei under an alternating acoustic pressure.

In comparison with other techniques, the major advantages of ultrasound are that it is nondestructive, rapid, and can easily be adapted for on-line measurements.

Despite its desirable attributes, ultrasound is not without deficiencies. It can be applied to systems that are concentrated and optically opaque. One of its major disadvantages is that the presence of small gas bubbles in a sample can attenuate ultrasound and the signal from the bubbles may obscure those from other components. Another potential problem occurs when ultrasound is used to follow complex biochemical and physiological events. In this case, it is difficult to attribute specific mechanisms to the observed changes in velocity and attenuation. In addition, velocity may strongly depend on the temperature of the foods, therefore in real processing operations with gradient temperature, it is critical to evaluate the effects of such gradients on the ultrasonic velocity measurements (Coupland, 2004; Povey, 1997).

F. ATOMIC FORCE MICROSCOPY

In 1986, Binning *et al.* provided a remarkable solution to the impossibility of molecular or submolecular resolution by scanning a sharp stylus attached to a flexible cantilever across a sample surface. This invention was known as AFM. This instrument is a new example of scanning probe microscopy (SPM) techniques in which the interaction between tip and specimen is not represented by a current deriving from tunneling electrons but rather by force interaction. The principle is very similar to the way in which a record stylus plays a record, with the exception that the stylus is much smaller (a few micrometers) (Kirby *et al.*, 1995). In the AFM, the stylus is rigidly fixed onto an elastic cantilever. When the stylus is close to the sample, the repulsive forces determine the bending away of the cantilever from the surface. By monitoring the extent of the cantilever bending, any undulations in the sample can be recorded and detected by a laser beam, which is reflected into a photodetector (Morris, 2004). The conventional microscopes look at samples, while the AFM feels the details on the surface of the specimen. The sample is felt by scanning it with a sharp probe attached to a cantilever or spring (Kirby *et al.*, 1995). Most AFM cantilevers are microfabricated from silicon oxide, silicon nitride, or pure silicon by applying photolithographic techniques. The sample is applied to a solid substrate, such as mica or glass, and its roughness dictates the restriction in the use of this technique.

Mica is a cleavable aluminum silicate crystal, whereas glass is a rougher substrate useful for imaging larger structures. Biopolymer samples are

generally applied onto cleaved mica and then air dried if a better resolution is to be realized. Solid samples can just be glued onto a metal plate before imaging. The force applied on the sample by the stylus is very important for determining the contrast. The movements of the samples in small 3D ranges are achieved by mean of piezoelectric devices. In general, there are two AFM-imaging methods, the contact mode and the noncontact mode. In the latter, the shearing forces exerted by the stylus scanning over the sample may be reduced or eliminated. In the contact mode, the atoms of the stylus are so close to the sample that they touch it. The most important contact mode of AFM imaging is that based on the constant repulsive forces on the cantilever, which are kept constant with a feedback circuit. When a variable force is exerted on the sample, the image is obtained by recording and amplifying the signal of the piezoelectric device. A particular imaging method, named ''error signal mode'' and suitable for emphasizing molecular structure of rough samples, involves the direct monitoring of the cantilever deflection as it senses features on the surface. In the contact mode, the forces on the sample are not always desirable because they can destroy the sample. This inconvenience can be solved by using the noncontact mode. In this case, the cantilever is bonded onto a small slab of piezoelectric material and then it is vibrated close to its resonant frequency. Images can be obtained in two distinct modes: true noncontact imaging mode, when the cantilever is vibrated so gently above the sample that it does not touch it, and tapping mode, when the cantilever is vibrated more strongly so that the stylus intermittently touches the sample. This last type of imaging attracts the interest of the users of this technique because it provides high resolution if compared to that obtained by performing the analysis by keeping both sample and cantilever immersed under a liquid and, furthermore, it does not require time for the instrument stabilization (Kirby *et al.*, 1995).

The AFM technique is easy to apply, the specimen can be imaged in air or liquid, the resolution is very high, and the sample preparation is much simpler if compared to those required by traditional microscopy.

AFM technique is able to provide information about the individual molecules of the material and the way in which size and shape of molecules affect their behavior in foods.

Biological nonconducting material can be easily imaged by AFM (Gunning *et al.*, 1996). AFM allowed the study of irregular polysaccharide structures and their function as suspending agents in foods (Kirby *et al.*, 1995). The polysaccharides were immersed in alcohol because the moisture present in the atmosphere can condense around the stylus or the surface of the samples, causing a poor quality image. By AFM in noncontact mode (tapping mode), Elofsson *et al.* (1997) characterized different whey protein preparations such as pure β-lactoglobulin standard whey protein concentrate and

cold gelling whey protein concentrate. The samples were diluted at three different concentrations, dried into mica sheets, and imaged in the AFM microscope. 3D views and cross-section topography images of monolayer coverage of β-lactoglobulin standard whey protein concentrate and heat-modified whey protein concentrate were obtained to clearly distinguish the different states of protein aggregation at a submicrometer level. In food context, AFM has also been used to study polysaccharide networks such as starch granules and cell walls from fruit and vegetables (Kirby *et al.*, 1995). AFM allows the study of interfacial phenomena, such as bacterial boils and fouling and air–water or oil–water interfaces, which stabilize emulsions or food foams. The technique provides the resolution suitable to visualize these structures and to study the surfactant-induced destabilization of protein-stabilized foams or emulsion, but it cannot be directly used to study interfaces in foods (Morris *et al.*, 1999). Moreover, AFM was used to visualize the internal structure of starch granules without inducing the necessary contrast in the images (Ridout *et al.*, 2002). The images allow the examination of the possible mutations that affect starch structure and its functionality.

G. VIBRATIONAL MICROSPECTROSCOPY

Raman microspectroscopy results from coupling of an optical microscope to a Raman spectrometer. The high spatial resolution of the confocal Raman microspectrometry allows the characterization of the structure of food sample at a micrometer scale. The principle of this imaging technique is based on specific vibration bands as markers of Raman technique, which permit the reconstruction of spectral images by surface scanning on an area.

While an optical microscopy gives only a mapping of the whole mixture, the Raman microspectroscopy offers selective image contrast of each molecular component because it uses a fixed wave number characteristic of each component of the mixture (Huong, 1996). Components larger than 1 μm can be illuminated by the micro-Raman setup and their spectra can be recorded without interference. The Raman spectroscopy measurements are a function of vibrations of all bonds, geometries, distances, angles, and polarizability of the chemical bonds. For these reasons, Raman spectroscopy can differentiate the single bond from the double or triple ones, whereas the other microscopy techniques give information only about the nature of the bonded atoms.

Also the infrared microspectroscopy (IR) is a vibrational spectroscopy, but it presents some differences with respect to Raman spectroscopy and also provides different information. In infrared spectroscopy the sample is radiated with infrared light, whereas in Raman spectroscopy a monochromatic visible or near infrared light is used. In this way, the vibrational energy

levels of the molecule are brought to a short-lived, high-energy collision state. The return to a lower energy state occurs by emission of a photon. Raman microspectroscopy is based on the detection of the vibrations of molecules whose polarizability changes, whereas IR spectroscopy detects vibrations of molecules whose electrical dipole moment changes (Thygesen *et al.*, 2003). The limiting spatial resolution is of the order of 1 μm × 1 μm in Raman microspectroscopy, whereas it is around 20 × 20 μm^2 in IR. Each food system shows characteristic absorbance bands for both Raman and IR microspectroscopy. The four major food chemical compounds (water, fat, protein, and carbohydrates) absorb in Raman and IR but with different intensities. For example, water presents very strong absorption in the IR but it is invisible in Raman spectroscopy because of the weak vibration of the O–H (Huong, 1996). FT-IR and Raman microspectroscopy may be combined with three different mapping techniques: point, line, and area. With point acquisition, several spectra are measured from different places in the sample. Line mapping defines a series of spectra along one dimension. Area-mapping technique uses two dimensions, providing a spectroscopic image that can be related to the corresponding visual image with an entire spectrum in each pixel. Raman technique is rapidly performed and does not require any destructive preparation of the sample, even if the sample could be destroyed due to the heating determined by the laser light (West, 1996). Compared with the infrared spectroscopy, it permits a better spatial resolution, an easier setting up, and in addition makes possible the focusing of a sample through a food-packaging material without exposing it to the atmosphere. Two important limitations of this technique are the signal-to-noise ratio, which can be very low if the sample fluoresces, and the fact that the surface of the sample cannot be planar to allow a correct evaluation of the repartition of each component (Huong, 1996). Raman and Infrared microspectroscopy may reveal useful information about food samples. Vibrational microspectroscopy was applied to a number of different problems related to food analysis to obtain information about microstructure and chemical composition. Samples of microscopic size can be directly analyzed in air, at ambient temperature and pressure, and under wet or dry conditions. By using confocal Raman microspectrometry, Piot *et al.* (2000) followed the evolution of protein content and structure during grain development of various wheat varieties. The technique is not only a powerful method to identify cereal components but it also gives information about the secondary structure and configuration of the proteins. The originality of the technique used in the work resides in the coupling between a Raman spectrometer and an optical microscope. The confocality was assured by a diaphragm located in the focal image plane of the sample, just before the input of the spectrograph. By using marker vibration bands, spectral images were generated on

one or more particular components. The whiter the points in the images, the more intense the Raman scattering was.

IR could represent a complementary technique with respect to Raman spectroscopy, to better understand structure and molecular bond at a micrometer scale (Wetzel *et al.*, 2003). The synchrotron infrared microspectroscopy is superior to the same technique using a conventional global as a source because it is 1000 times brighter and highly directional and there is no thermal noise. Nevertheless, it is also more expensive. The vibrational microspectroscopy was applied to other different heterogeneous food systems providing information about the microstructure (Thygesen *et al.*, 2003). For example, high-quality spectra of starch granules in potatoes were acquired. Using Raman microspectroscopy it was possible to study the distribution of amygdalin in bitter almond cotyledons. IR microspectroscopy was used to study the nature of the blisters contained on bread crust or microstructure of high-lysine barley.

H. PHASE-CONTRAST MICROTOMOGRAPHY

Tomography is usually defined as the quantitative description of a slice of matter within an object. Several sources can be used, in particular X-rays sources, widely used in both the medical and industrial fields. The experimental implementation of tomography requires an X-ray source, a rotation stage, and a radioscopic detector.

A complete analysis is made by acquiring a number of radiographs (typically about 1000) of the same sample under different viewing angles (one orientation for each radiograph). A final computed reconstruction step is required to produce a 3D map of the linear attenuation coefficients in the material. This 3D map indirectly gives a picture of the structure density. In the X-ray-computed tomography, the X-ray source and detector are placed at the opposite sides of the sample. The spatial resolution of the attenuation map depends on the characteristics of both the detector and number of X-ray projections.

X-rays can be absorbed or scattered and the attenuation of the incident radiation can be expressed by the Beer's law:

$$I = I_0 \cdot \mathrm{e}^{-\int_l \mu(x)\cdot \mathrm{d}x}$$

where I and I_0 are the transmitted and incident radiation, respectively, μ is the linear attenuation coefficient (cm^{-1}), and l (cm) is the path of the radiation inside the sample. As a consequence, the obtained image is a map of the spatial distribution of the μ in which the brighter region corresponds to the higher level of attenuation if the detector used is a CCD

camera. Differences in the linear attenuation coefficients within a material are responsible for the X-ray image contrast.

The main contrast formation in X-ray tomography is due to absorption contrast. This is often a limitation for imaging of low-Z or low-density materials. Synchrotron radiation (SR) sources are, essentially, large multidisciplinary research facilities supporting a broad research portfolio in physics, chemistry, biology, and engineering. These sources are based on high-energy electron accelerators producing electromagnetic radiation that covers a wide spectral range from the far infrared to hard X-rays. Compared with conventional laboratory sources, SR can deliver several orders of magnitude greater photon flux with a well-collimated beam and other properties that make them extremely powerful tools for a whole range of scientific and technological applications.

Advances in electron storage ring and the use of the so-called insertion devices (wigglers and undulators) have led to the development of third generation sources with another important characteristic: the small divergence of the beam as seen from the sample, due to the very small area of the electron beam that acts as the source of SR, combined with the increased distance between the source itself and the sample. These qualities of the X-ray beam, defining its spatial coherence, have been used to offer new opportunities in the field of X-ray imaging, such as phase-contrast and diffraction-enhanced imaging.

When X-rays interact with any kind of materials, *absorption* and *phase shifts* effects occur. Conventional X-ray radiography relies on the *absorption properties* of the sample. The image contrast is produced by a variation of density, a change in composition or thickness of the sample, and is based exclusively on the detection of an *amplitude variation of X-rays* transmitted through the sample itself. Information about the phase of X-rays is not considered. The main limitation of this technique is the poor intrinsic contrast in samples with low atomic number (i.e., the case of "soft matter") or in materials with low variation of absorption from point to point.

If X-ray beams have a high spatial coherence—as for third generation SR sources–contrast may be originated by the interference among parts of the wave front that have experienced different *phase shifts* through the sample (Fresnel diffraction). In the energy range of 10–25 keV, the phase shift contribution can be up to 1000 times greater than the absorption one and allows the detection of the phase effects even if the absorption contrast is low (Cloetens *et al.*, 1996; Snigerev *et al.*, 1995). Among the different techniques available for phase-sensitive imaging (Fitzgerald, 2000), the PHase contrast (PHC) microtomography setup is the same as that of absorption microtomography with the difference that the detector is positioned at a certain distance d from the sample. The choice of d depends on the size a of the

feature to be identified, measured perpendicularly to the beam direction. In the edge detection regime ($d \ll a^2/\lambda$, where λ is the X-ray wavelength), images can be directly used to extract morphological information. Larger values of d lead to the holography regime ($d \approx a^2/\lambda$), and have not been used here. In the images, the Fresnel diffraction pattern appears superimposed to the absorption contrast and contributes strongly to enhance the visibility of the edges of the sample features.

The main limitation of tomographic setups based on conventional X-ray generators is obviously related to the lower flux in comparison with synchrotron radiation sources. As X-ray tubes generate a polychromatic spectrum, moreover, the different attenuation of photons as a function of their energy leads to a fast attenuation of the less energetic photons and, as a consequence, to an increase of the mean energy along the path of the X-rays. This effect, called "beam-hardening," generates different kinds of artifacts that must be taken into account during the reconstruction or, better, during the data acquisition (Kaftandjian *et al.*, 1996).

Conventional systems, on the other hand, have their own advantages. First, the access to such systems is much easier than to a synchrotron. Second, they can deliver X-rays with higher energies compared with typical SR sources, with evident advantages when bulky or high-Z samples are considered. Finally, thanks to the last generation of scanners based on micro- and nanofocus generators, the space-resolving power of these equipments has increased dramatically (Hirakimoto, 2001).

According to Evans (1995), differentiation of features within the materials is possible because μ at each point directly depends on the electron density of the material in that point (ρ_e), the atomic number (Z) of the chemical components of the materials in that point, and the energy of the incoming X-ray beam (I_0). In particular, the linear attenuation coefficient can be approximately considered as the sum of the Compton scatter and photoelectric contributions:

$$\mu = \rho_e \times \left(a + \frac{bZ^{3.8}}{I_0^{3.2}} \right)$$

where b is a constant (Vinegar and Wellington, 1987), a is the weakly energy-dependent Klein–Nishina coefficient (related to the angular distribution of the scattered photons as a function of the initial energy), ρ_e is given by $\rho_e = \rho \cdot (Z/A) \cdot N_{AV}$ (where ρ is the material density, Z and A are the atomic number and atomic weight, respectively, and N_{AV} is the Avogadro's number). The first term in the above equation represents the Compton scattering (direction change with loss of energy), which is predominant at X-ray energies above 100 keV, whereas the second term accounts for the

photoelectric absorption (deposition of all energy in the matter), which is predominant below 100 keV (Vinegar and Wellington, 1987). Therefore, when various parts of the sample display contrast in density, these parts will be characterized by distinct values of the linear attenuation coefficient and differentiated regions contrasting brightness in the CT image.

Spatial distribution of the linear attenuation coefficients within material is based on the average linear attenuation coefficient along the projected line through the sample that can be calculated from the measured X-ray intensities as follows:

$$\bar{\mu} = \frac{\ln\left(\frac{I}{I_0}\right)}{-N \cdot \Delta x} I_0 \times e^{\mu \cdot x}$$

where $\bar{\mu}$ is the average attenuation coefficient in 1/cm and I/I_0 is the normalized X-ray intensity. The length of the projection is a constant approximated by the product of the step size (Δx) and the number of steps (N).

In the case of conventional sources, the ability to discriminate among materials with closely similar linear attenuation values (or bulk density) strongly depends on the accuracy of the μ_{voxel} value determination (Denison *et al.*, 1997). For each individual object voxel within a digital image, it is possible to compute a normalized attenuation coefficient known as *CT number* from the linear attenuation:

$$\text{CT number} = k \cdot \frac{(\mu_{voxel} - \mu_{water})}{\mu_{water}}$$

where μ_{voxel} is the linear X-ray absorption coefficient of a given matter expressed in 1/m, μ_{water} is the linear X-ray absorption coefficient of water in 1/m, and k is a constant value. In the case of $k = 1000$, the CT number is called "Hounsfield unit." It has an arbitrary scale in which a CT number of -1000 is attributed to air and a CT number of zero is attributed to water. This parameter allows the obtainment of relative measures of structural features.

The measurements obtained by a CT scanner results in a series of attenuation coefficients that are function of position and angle $\mu(t, \theta)$. Computer manipulation is required to convert these physical data into digital image arrays $g(x, y)$ in order to determine the distribution of the attenuation coefficients and hence the density distribution within the sample. There are many different algorithms developed to accomplish this task. One of most popular used today is called "filtered backprojection" algorithm (Hermann, 1980; Kak and Slaney, 1988) that is the base of the reconstruction software programs conventionally used to obtain 2D and 3D images. Figures from 1 to 5 show examples of both reconstructed 2D and rendered 3D images of porous and cellular food products obtained by SR X-ray absorption microtomography.

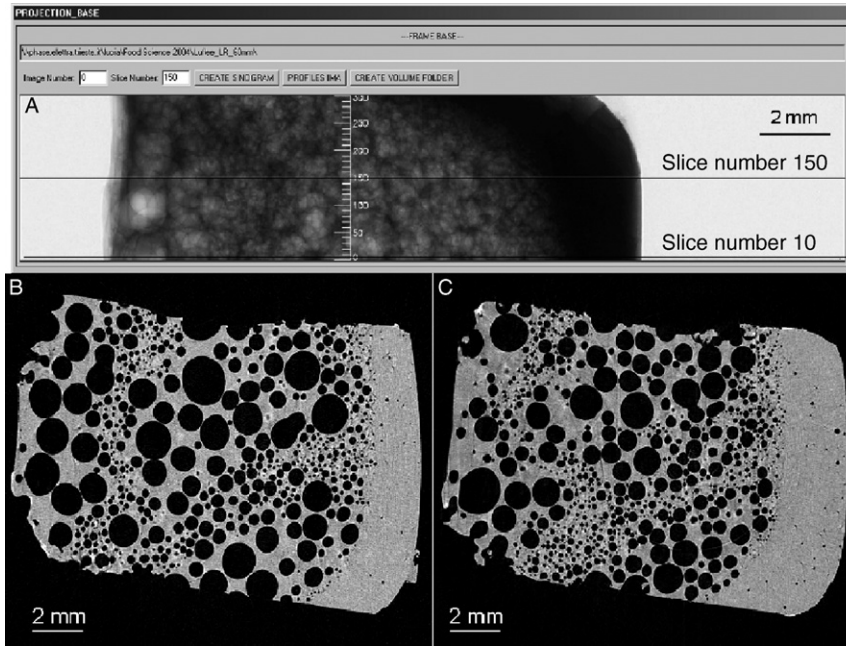

FIG. 1 3D X-ray microtomographic (XRM) images of a milk aerated chocolate bar. (A) X-ray absorption radiograph, (B) reconstructed slices corresponding to the slice number 10 within (A), (C) reconstructed slices corresponding to the slice number 150 within (A). The images show a closed cell structure at microscopic level (pixel size = 14 μm, $E = 13$ keV).

The attenuation along a line through the sample is calculated. This procedure simply assigns the mean attenuation coefficient to each point (or pixel) along that line. This backprojection is repeated for all angles. The attenuation coefficient for a particular point will be built up from all the projections passing through that point (or pixel). Nevertheless, the image under reconstruction is not continuous but composed of discrete pixels. The projection lines will not pass perfectly through the center of each pixel in their path and therefore a mathematical method is used to describe the projection line in terms of individual pixels within a matrix.

The reconstruction algorithms to be used for conventional sources are substantially different from the codes described in the previous section, due to the different acquisition geometry related to the conical shape of the beam (Burch and Lawrence, 1992; Feldkamp *et al.*, 1984).

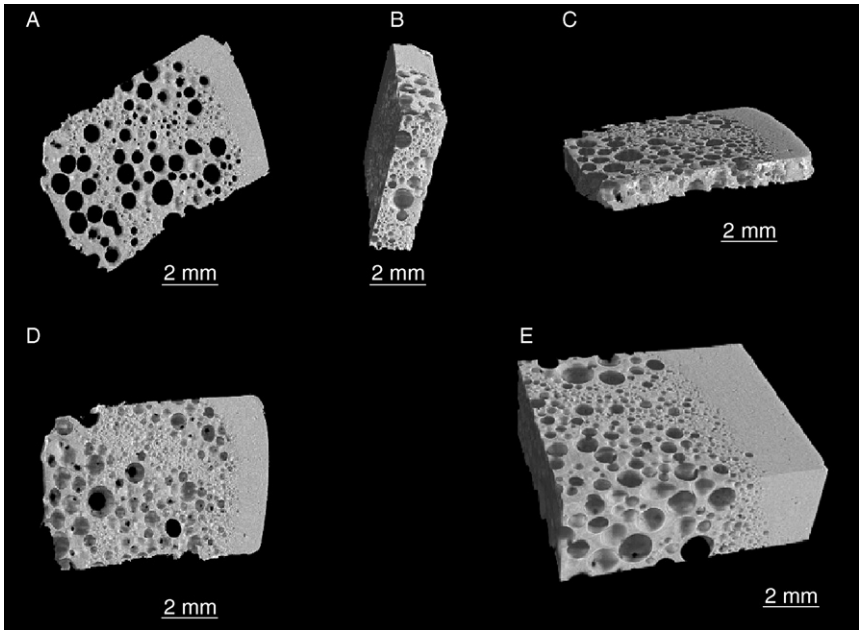

FIG. 2 3D XRM images of a milk aerated chocolate bar at middle level of sample. Rendered volumes numerically cut with (A) 20 slices, (B) 200 slices, (C) 100 slices, (D) 60 slices, and (E) 200 slices. The numerically rendered models reveal the foamed structure of sample from different angles of view (pixel size = 3.85 μm, $E = 13$ keV).

III. DATA PROCESSING

A. COMPUTERIZED SIMULATIONS OF X-RAY IMAGING TECHNIQUE

In order to use the X-rays in a wide range of application areas of agricultural and food industry, it is necessary to optimize the ability of the detection system in determining small spatial density and/or atomic number differences within a specific food substrate. For each specific application, there is generally a complex task to design the appropriate optimal parameter values such as the current and voltage of the X-ray tube, the geometric adjustment, the exposure time, and so on.

There is an increasing interest in the simulation codes of X-rays interactions with samples with the purpose to develop and optimize new imaging systems and to assess the influence of the various adjustable parameters in

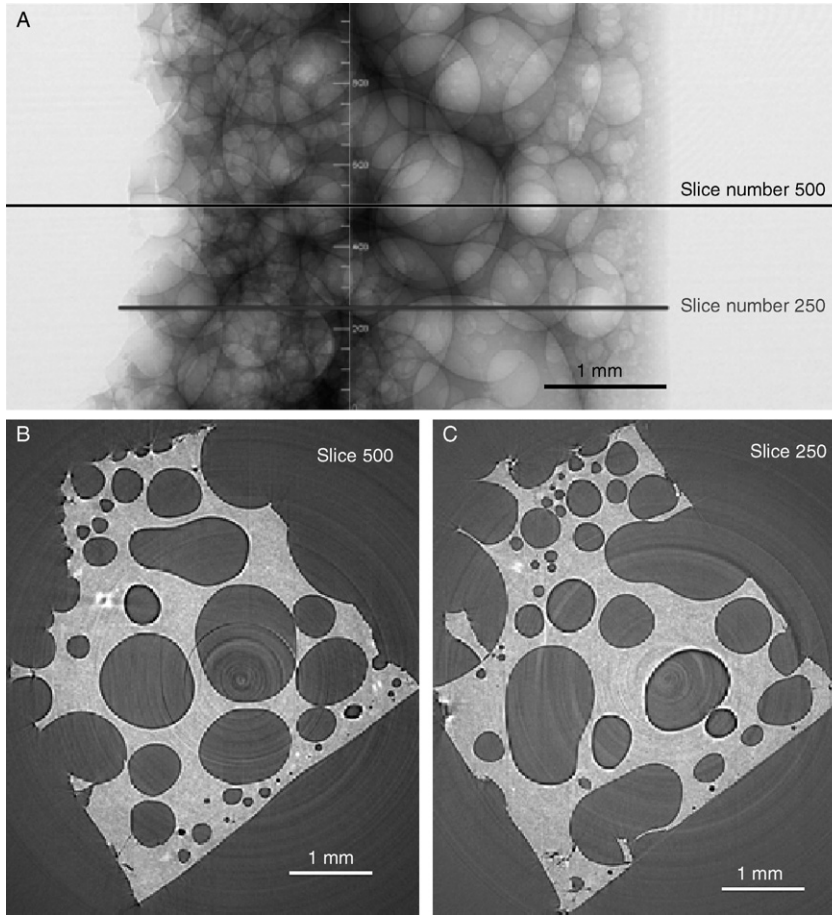

FIG. 3 Milk aerated chocolate bar. (A) X-ray absorption radiograph, (B) reconstructed 2D XRM images corresponding to the slice number 500 within (A), (C) reconstructed 2D XRM images corresponding to the slice number 250 within (A).

the image formation (Duvauchelle *et al.*, 2000; Zwiggelaar *et al.*, 1996). This approach allows to choose the most suitable components and to predict the future device performance by acting as a virtual experimental bench. Simulated images that can be obtained in little time and at low cost may enable the behavior of the whole imaging system to be investigated in complex situations (Inanc *et al.*, 1998).

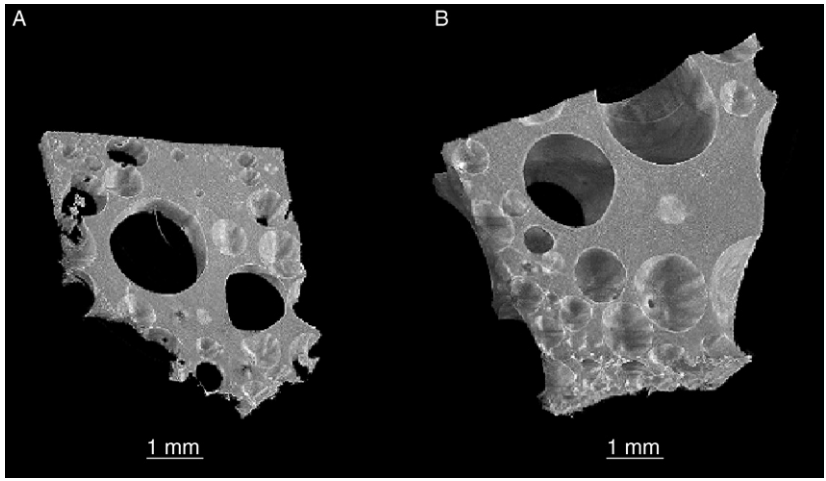

FIG. 4 3D XRM images of a milk aerated chocolate bar at middle level of sample revealing its foamed structure. (A) Rendered model numerically cut with 100 slices. (B) Rendered model numerically cut with 200 slices (pixel size = 3.85 μm, $E = 13$ keV).

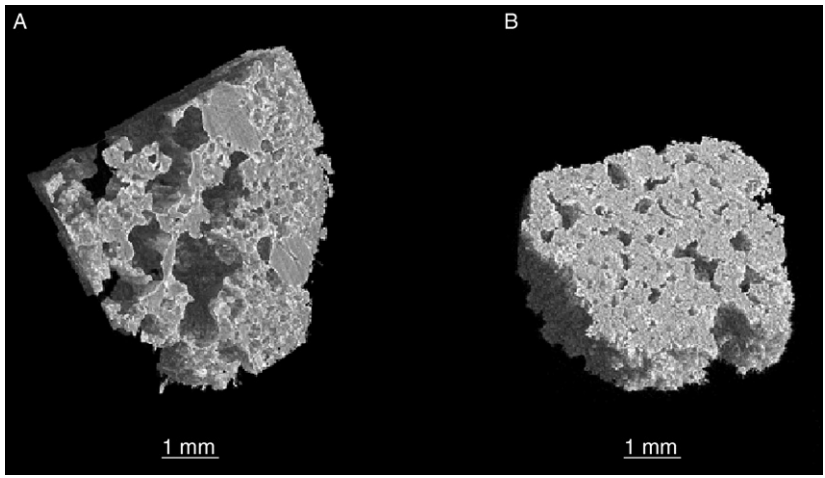

FIG. 5 3D XRM images of samples of commercial (A) and home made (B) crust pastry biscuits. Rendered volumes from (A) 300 and (B) 200 reconstructed slices (pixel size = 3.85 μm, $E = 13$ keV). It is worth noting a highly interconnected sponge-like structure: air cells are open and with highly irregular edges highlighting a coarse structure in the commercial sample and fine structure in the home made one.

Zwiggelaar *et al.* (1996) developed a specific computer code named XCOM/EGS4 to optimize the X-ray detection with respect to the following aspects: energy/dose ranges useful to detect variation in density and chemical composition, trade-off between signal-to-noise and intensity as a function of energy, and optimum energy range. XCOM/EGS4 code could be used to determine the optimal imaging conditions in more specific problems such as the foreign body detection or 3D distribution of chemical constituents. Possible application areas are the meat industry (control of the fat/meat ratio), potato industry (starch and sugar contents), and fruit quality assessment (sugar content, bruising, and problems such as hollow heart). Simulation of X-ray techniques using scattered photons could find applications in food processing to predict the structure development in baking process or the crystallization during cooling (Zwiggelaar *et al.*, 1996).

Another computer code was developed by Duvauchelle *et al.* (2000) to simulate the tomographic scan. Simulation is based on ray-tracing techniques and X-ray attenuation law. Automatic translations or rotations of the object can be performed to simulate tomographic image acquisition. Simulations can be carried out with monochromatic or polychromatic beam spectra. The simulation principle is completely deterministic and consequently the computed images present no photon noise. This computer code was designed to accept standard computer-aided drawing (CAD) files describing the sample geometry. The use of CAD models is a helpful tool to enable simulations with complex 3D samples since the geometry of every component of the imaging chain, from the source to the detector, can be defined. Geometric sharpness, for example, can be easily taken into account, even in complex configurations. Many software packages enable complex 3D objects to be drawn and CAD files to be generated in a short time, for example, with the stereolithographic (STL) or unstructured cell data (UCD) format. These files contain a list of nodes and meshes (triangular facets) that fit the object surface. The precision of this fit, which is linked to the size of the meshes, can be adjusted. The object may consist of different parts, possibly made of different materials, assumed to be homogeneous. The CAD model of each part can be independently handled. If a compound material is specified, the corresponding mass attenuation coefficient μ/ρ is calculated with the well-known formula

$$\frac{\mu}{\rho} = \sum\nolimits_i \omega_i \left(\frac{\mu}{\rho}\right)_i$$

where the index i refers to each element of the compound and ω_i stands for the fraction by weight associated to the element i.

B. CT NUMBER AND FOOD QUALITY

Food quality inspection is extremely important in current agricultural production. X-ray CT technique shows a great potential for nondestructive, online sorting of immature from mature fruits (Brecht *et al.*, 1991; Yantarasri *et al.*, 2000). For example, X-ray-computed tomographic (CT) scanner was used to monitor and predict the internal quality changes in peaches during ripening (Barcelon *et al.*, 1999). As ripening time increased, the region surrounding the peach stone became drier and contained voids (dark region in the image) as showed by the low X-ray absorption and negative value of the CT number. The CT number was calculated on the radial and longitudinal cross-sections of the peach CT images. A histogram was produced reflecting the frequency of the CT number of each peach slice. Authors satisfactorily determined the relationships between the CT number and peach characteristics such as moisture, density, soluble solids, pH.

Yantarasri *et al.* (2000) observed significant differences between durian fruit of 50% maturity (CT number −70.59) and durian fruit of 80% maturity (CT number −45.18). The CT number computed from the image intensity showed an increasing trend with the increase in maturity according to a polynomial relationship with $R^2 = 0.99$. Brecht *et al.* (1991) reported similar results in tomato in which X-ray CT images showed intense signal in the gel tissue of fully mature tomatoes that appeared brighter than that of immature fruit. Suzuki *et al.* (1994) reported CT number referred to unripened papaya lower than that of the ripened ones.

X-rays have been used to detect structural discontinuities caused by voids and cracks and density variation. X-ray line scans were used to determine bruising, density, and water content of apples (Diener *et al.*, 1970; Tollner *et al.*, 1992), to select mature lettuce heads (Lenker and Adrian, 1971), and to detect hollow heart in potatoes and split pit in peaches (Han *et al.*, 1992). X-ray-computed tomography has also been used to detect density changes in tomatoes (Brecht *et al.*, 1991), seeds in oranges and pommels (Sarig *et al.*, 1992), defects in watermelons and cantaloupes (Tollner, 1993), internal changes of peaches, and stones in apricots (Zwiggelaar *et al.*, 1997). Tomographic images have been numerically analyzed to assess the quality of small food structures such as tomato seedlings (Van der Burg *et al.*, 1994), kernels (Schatzki and Fine, 1988), and walnuts (Crochon *et al.*, 1994). 3D numerical reconstructions by CT techniques have been used to obtain the density distribution and water content of apples. This technique has also been applied to determine injury by vapor heat treatment in papaya (Suzuki *et al.*, 1994), woolly breakdown in nectarines (Sonego *et al.*, 1994), internal defect disorder of durian, mangosteen, and mango (Yantarasri and Sornsrivichai, 1998; Yantarasri *et al.*, 1997), dry juice sac and granulation

of tangerine fruits (Yantarasri and Sornsrivichai, 1998), and internal bruising and ripeness of pineapple (Yantarasri *et al.*, 1999).

Computed tomography offers a great potential for nondestructive studies of transport phenomena in foods. For example, accurate quantification of salt concentration in cured pork was made by computed tomography relating the CT values to the chemical analysis of salt (Vestergaard *et al.*, 2004).

C. CT NUMBER AND FOOD SAFETY

Patel *et al.* (1996) developed a strategy to process X-ray images with the purpose of detecting internal inhomogeneities in food products due to foreign objects including stone, metal, and glass. Food substrates in X-ray image show high textured appearance but contaminants or defects do not necessarily exhibit different textural properties. To overcome this problem, authors used a convolution-based method to detect anomalies within the texture of the food background. The convolution masks acted as matched filters for several types of textural variation found in the image. The convolution operation transformed the digital data from the spatial domain to the feature space domain allowing the highlighting of each local texture properties. This approach was able to recognize very small foreign objects or defects of 2×2 pixel size from the rest of the textured food substrate.

D. INTERNAL FEATURES AND MECHANICAL PROPERTIES

X-MT proved to be a very useful technique to image the 3D microstructure of cellular and porous food products (Falcone *et al.*, 2004a,b; Lim and Barigou, 2004; Schatzki and Fine, 1988; Tollner *et al.*, 1992; Van Dalen *et al.*, 2003; Van der Burg *et al.*, 1994). Effective numerical algorithms are developed to derive some important structure descriptors from digital images such as local density, volume fraction, specific surface (Falcone *et al.*, 2004b; Lim and Barigou, 2004; Maire *et al.*, 2003), spatial cell size distribution, cell wall thickness distribution (Lim and Barigou, 2004; Maire *et al.*, 2003), index of connectivity of the pores (Lim and Barigou, 2004), fractal dimension (Falcone *et al.*, 2004a), cell wall number, cell wall thickness, cell wall spacing, anisotropy degree of the solid phase, and main orientations of the cell walls in the space (Falcone *et al.*, 2004b). Approximate information on volume fraction, cell wall thickness, and cell size can be obtained using conventional 2D image analysis techniques (Whitworth and Alava, 1999), but information about anisotropy degree, predominant orientation of the structural elements, and index of connectivity requires the use of 3D data to obtain a correct quantification.

1. *Volume fraction*

Both 2D and 3D image analysis allows to get quantitative information on the volume fraction in foamed foods including air cell count, total cell area, relative cell area, and pore volume, but the 2D approach results in great limitations. Lim and Barigou (2004) extracted data concerning the above features from reconstructed CT images of foamed foods such as foamed chocolate bar, honeycomb chocolate bar, chocolate muffin, marshmallow, and strawberry mousse. They worked to provide a quantitative comparison between two commercial softwares, that is, the T-View software package (Skayscan, Belgium, 2003) used to analyze 3D images and the Leica Q-Win Pro image analysis software [Leica Microsystems (UK) Ltd., 2000] used to analyze 2D images. Both the software packages were run only on the central area of each image, about 42 mm^2, excluding the sample edges that had been affected by the physical cutting. In general, the T-View software allows to detect more air cells than the Leica Q-Win Pro image analyzer. This arises from the fact that, in its automatic object measurement mode, the image analysis of the Leica software did not include those parts of the cells situated on the borders of the measurement region, whereas the T-View software also included these incomplete cells. However, the bi-dimension cell parameters measured by the two methods are in close agreement, with a mean difference of 12% in relation to the cell size and less than 1% in the relative area. The smallest difference in the values of the relative area measured by the two methods is due to the fact that the automatic field measurement mode of the Leica software measures the whole cell areas detected in the region of interest in the same way as the T-View software. Falcone *et al.* (2004b) developed an algorithm able to perform the stereological analysis of the CT images and used it in order to evaluate the bread crumb porosity. The results were compared with those obtained by means of the ImageJ software package (version 1.29, National Institute of Health, USA, in the public domain from http://rsb.info.nih.gov/ij site at April 16, 2003). Authors found that the observed differences between the solid volume fractions as calculated by means of the two software packages were not statistically significant.

Advances in 3D image analysis can be attributed to Maire *et al.* (2003) who quantified the local volume fraction of bread crumb samples by means of the 3D image analysis. It is known that the gray level in each voxel of a tomographic image is proportional to the local density of the constituents so that it can be directly used to quantify the global and also the local value of the density in a foamed food. According to Maire *et al.* (2003), global density does not provide enough information to characterize cellular architecture of bread. For this purpose, density profile or local density variation

can be more interesting. These authors investigated the local density variation in bread crumb by determining the histogram of the local density. For each voxel of the volume, they calculated an average gray level of the tomographic images considering the neighboring voxels in a predefined box of size $N \times N \times N$. The choice of the value of N was made according to the characteristics of the architecture of the bread crumb. N was taken larger than the mean cell size and smaller than the size of the volume studied. This approach allows to take into account all the incomplete cells within an image. N value was thus chosen by means of the following equation:

$$N = \frac{-\pi d^3}{6(1-\rho)} \sqrt{\sqrt{1/3}}$$

where d is the mean cell size and ρ is the relative density of bread crumb.

2. *Cell size distribution*

Thanks to the high resolution of the tomographic 3D images, it is possible to accurately calculate the cell size distribution (Lim and Barigou, 2004; Maire *et al.*, 2003). Conventional 2D image analysis allows to get a more approximate evaluation of the cell size distribution than 3D image analysis. To perform this calculation, it is necessary to isolate each cell considered as a cluster of connected voxels separated from the others (i.e., each cell does not have voxel connection with the other cells). Once each cell is isolated, standard morphological information can be obtained by using conventional image analysis techniques. Saltykov area analysis method or other techniques are usually applied to calculate 3D parameters on cross-section tomographic images. This approach gives good results only if a simple shape (spherical or convex) can be assumed for each cell (DeHoff and Rhines, 1972). This technique cannot be satisfactorily used for the analysis of sponge-like materials, such as the bread crumb, (Maire *et al.*, 2003) due to the number of the open gas cells that is greater than that of the closed ones. The same consideration can be made for the cellular-like foods whose resolution image setup is not enough to resolve the cell walls within internal structure or also when the segmentation process is not adequate to preserve the whole portion of the image that is related to the continuous solid phase.

The cell size distribution is very easy to get if the cells are perfectly closed. If the closed cells are connected, the cell size distribution can be determined according to two methods (Maire *et al.*, 2003). The first possibility is to try to close the cells within the digital image using morphological operations such as erosion/dilation. When this activity is done successfully, it is possible to extract some morphological 3D parameters of cells such as volume, surface, aspect ratio, and sphericity. The cell size distribution can be easily obtained

since the size is calculated for each cell. The second possibility is to use morphological operations, for example, opening granulometry, to directly retrieve the cell size distribution from the image. This technique can be also applied on 3D images allowing, in this way, the measurement of the size distribution even if the cells are connected. The method is applied by placing virtual spheres having a different radius within digital arrays representing the solid microstructure. Obviously, it works well if the cells are equiaxed. Otherwise, only the smallest dimension of the cell is retrieved. This method is particularly interesting in the case of the bread crumb or of other sponge-like structures for which morphological closing would be completely impossible. Authors determined the normalized volume frequency of the cell size for bread crumb. Opening granulometry technique can be used not only to quantify a cell size distribution but also a wall thickness distribution. This technique, instead, does not supply information on the cell shape.

Another approach to evaluate the cell size distribution is the Saltykov area analysis of the CT images that is based on the stereological measurement of the 2D cell areas (Lim and Barigou, 2004). Authors determined the volume cell size frequency for foods such as foamed chocolate bar, honeycomb chocolate bar, chocolate muffin, marshmallow, and strawberry mousse. A foamed food can be considered as an idealized polydispersed system of suspended spherical or convex particles. A test plane, which cuts the system, will encounter circular sections of different sizes. The basic idea in the Saltykov area analysis is to work backward from this distribution of 2D circular sections to the real spatial size distribution of 3D particles. The circular sections may or may not coincide with the particle diameters, so the source of each section must be determined. For nonidealized particle systems, this method generally assumes that all particles are spherical and that the distribution of particle size can be represented by a discontinuous distribution. The Saltykov stereological technique provides a function based on the probability of random planes intersecting a sphere of diameter D to give sections of diameter d. Provided that the number of classes is not too small, the greatest inaccuracies are expected to arise from nonspherical particles. The assumption of sphericity, however, is usually found to be satisfactory for spheroidal and equiaxed particles.

According to Underwood (1970) and Xu and Pitot (2003), the general Saltykov working formula is the following:

$$(N_v)_j = \frac{1}{D_j}\begin{bmatrix} +1.6461(N_A)_j & -0.4561(N_A)_{j-1} & -0.1162(N_A)_{j-2} \\ -0.0415(N_A)_{j-3} & -0.0173(N_A)_{j-4} & -0.0079(N_A)_{j-5} \\ -0.0038(N_A)_{j-6} & -0.0018(N_A)_{j-7} & -0.0010(N_A)_{j-8} \\ -0.0003(N_A)_{j-9} & -0.0002(N_A)_{j-10} & -0.0002(N_A)_{j-11} \end{bmatrix}$$

where $(N_v)_j$ is the number of particles per unit of sample volume in the class interval j; D_j is the actual diameter of the particle in the class interval j; $(N_A)_j$ is the number of circular sections in the class interval j per unit of cross-section sample area; $(N_A)_{j-1}, (N_A)_{j-2} \ldots (N_A)_{j-11}$ are the number of circular sections in successively smaller size intervals $j-1$, $j-2$, …, $j-11$, found per unit of cross-section area. In this formula, j has an integer value ≤ 12, that is, the method uses a maximum of 12 class intervals to construct the particle size distribution.

In order to specify the size of a circular section, instead of the absolute area A, the Saltykov method adopts the ratio $A/A_{\max}$, where $A_{\max}$ is the maximum circular section area in the whole population. The first step in determining the cell size distribution is to measure all the 2D circular sections, identifying the largest cell section in the total cell section population found on the section planes. This maximum area can be used to divide the size distribution of the cell sections into 12 classes and to determine the total number of sections in each class.

Lim and Barigou (2004) used a scale factor to determine the class intervals for $A/A_{\max}$ based on a logarithmic scale of diameters with a factor of $10^{0.1}$ (=0.794). Consequently, a logarithmic scale with a factor $(10^{0.1})^2$(=0.631) is used by authors for the sectional areas. In their study, a total of 1293 cell sections were traced on 41 horizontal slice images with a spacing of 0.189 mm. The maximum section area in the whole population of the cell sections was found to be equal to 3.83 mm^2, giving a maximum section diameter of 2.209 mm. After grouping all the circular sections into 12 class intervals, the Saltykov working formula was used to convert this 2D information into a 3D bubble size distribution. Thus, the number of particles per unit of volume in the largest class interval $j = 1$ was given by

$$(N_v)_j = \frac{1}{D_j}\left[1.6461(N_A)_1\right] = \frac{1}{0.2209}[1.6461(2)] = 15$$

where D_j is expressed in cm, $(N_A)_j$ is expressed as bubble cm^2, and $(N_v)_j$ is expressed as bubble cm^3. For the smaller bubble size intervals, the procedure is similar except that for the subtraction of the number of those sections contributed by the spheres in the previous classes. Therefore, for $j = 2$, the calculation proceeded as follows:

$$\begin{aligned}(N_v)_j &= \frac{1}{D_j}\left[1.6461(N_A)_2 - 0.4561(N_A)_1\right] \\ &= \frac{1}{0.1755}[1.6461(6) - 0.4561(2)] \\ &= 51\end{aligned}$$

The calculations are then carried out for the remaining class intervals until all particle cross-sections have been accounted. It is worth noting that for each class interval, the value of D used in the calculation was that of the largest section in the interval. The accuracy of the stereological analysis was checked calculating the total volume of the air cells in each distribution: the maximum difference observed was about 4%. Authors found three apparent peaks in the 3D cell size distribution relative to the aerated chocolate. The first peak around 0.2 mm represented the population of the smallest bubbles interdispersed between the larger ones, the second peak around 0.4 mm represented the population of medium size cells near the top and bottom regions of the chocolate foam, the third peak around 1.4 mm represented the population of the largest cells contained within the bulky foam structure. Such a cell size distribution was best fitted by a three-parameter gamma distribution according to the following probability density function:

$$f(x) = \frac{(x-\vartheta)^{a-1}\left(\mathrm{e}^{-(x-\vartheta)/b}\right)}{\Gamma(a)b^a}$$

where $a = 1.0015$ is the shape parameter, $b = 0.5795$ is the scale parameter, $\vartheta = 0.1381$ is the threshold parameter, and Γ is the gamma function. Concerning the honeycomb chocolate sample, the cell size distribution data were best fitted by a lognormal distribution according to the following probability density function:

$$f(x) = \frac{\mathrm{e}^{[\log((x-\vartheta)-\zeta)^2/2\sigma^2]}}{(x-\vartheta)\sqrt{2\pi\sigma}}$$

where $\sigma = -1.8284$ is the location parameter, $\zeta = 1.2719$ is the scale parameter, and $\vartheta = 0.2432$ is the threshold parameter.

The cell size distribution in products, such as marshmallow, muffin, and mousse, was also fitted by a lognormal distribution.

3. *Cell wall thickness distribution*

The technique described in the previous section can be easily applied also in the analysis of the solid phase (Maire *et al.*, 2003). Closed cell foams can be generally described with edges and walls. An important morphological parameter is the solid fraction contained in the cell edges "ϕ" that is used in some mathematical models (Gibson and Ashby, 1997). A value of ϕ equal to 1 indicates that the foam presents open cells. In order to measure this parameter, it is very sensitive the resolution used during the image acquisition and also the segmentation performed on the digital volume. Sometimes, when the edges and the walls present two different values of thickness,

a bimodal distribution is observed: the distribution showing the lowest values corresponds to the cell wall thickness distribution, whereas that showing the highest values corresponds to the edges thickness distribution. The case in which the deconvolution is feasible, the value of ϕ corresponds to the integral of the second peak. The latter represents the edges divided by the integral of the total curve.

4. *Degree of anisotropy*

Anisotropy primarily derives from the spatial arrangements of the structure elements or particulates and manifests itself in the directional dependence of both mechanical and transport properties. Anisotropy degree is a measure of the 3D structural symmetry, indicating the presence or absence of a preferential alignment of the structure elements along a particular direction. The anisotropy quantification primarily has importance in the modeling of the mechanical behavior of a cellular or porous structure (Odgaard, 1997). For many porous materials, the structural anisotropy is quantified by a "fabric" measure (Cowin, 1985; Kanatani, 1984) that represents the preferential orientations of the cell walls and the degree of dispersion of the solid phase around the main directions. The analysis of the anisotropy consists of a numerical approach based on the stereological calculus and also on the anisotropy tensor eigenanalysis of direction-dependent structural descriptors such as the mean intercept length (Harringan and Mann, 1984; Whitehouse, 1974), the star length distribution, and the star volume distribution (SVD) or areal pore size (Inglis and Pietruszczak, 2003).

Computerized algorithms were developed in order to perform the stereological calculation on natural materials such as soil, trabecular bone (Kuo and Carter, 1991; Odgaard, 1997; Odgaard *et al.*, 1997; Pietruszczak *et al.*, 1999; Whitehouse, 1974), and manufactured fabric materials such as sedimentary rocks and reinforced composites (Kanatani, 1985; Pietruszczak and Mroz, 2001). The basic idea is that, for each considered angle, many parallel lines are sent in order to cover the whole test volume and the mean intercept length is calculated as the average for all these lines. In the case of the isotropic objects, lines traversing the object at any angle will pass through a similar length of the solid phase. Anisotropy tensor eigenanalysis is then used to extract some numerical parameters that define orientation and anisotropy of these mean intercept length distributions. In the case of the orthotropic materials, a mathematical relationship exists between morphological features (volume fraction and fabric measures) and elastic properties (Young's modulus, shear modulus, and Poisson ratios) (Cowin, 1985). This is a general finding based on the experimental evidence that the anisotropy tensor main orientations correspond to the mechanical main orientations of these materials.

The bread crumb is an anisotropic material, as suggested by the fabric tensor value (Falcone *et al.*, 2004b). Authors proved that the volume fraction (in terms of porosity or density), which is a first measure of the bread architecture, cannot predict the compressive elastic modulus and a measure of the "structural anisotropy" must be performed. They used a CT scanner able to obtain high-contrast tomographic images with a nominal resolution of 14 μm along each edge of the voxels in the 3D arrays. The high performance of the CT system used allowed to successfully resolve the whole 3D map of the solid phase of the bread crumb. Authors used a numerical procedure able to perform an accurate characterization of the internal microarchitecture of the bread crumb (Falcone *et al.* 2004b). They obtained some direction-dependent measurements (basic quantities) by probing segmented 3D images with an appropriate volumetric array (3D testing sphere) of parallel test lines. The obtained directional data were used to derive a specific anisotropy descriptor named "mean intercept length vectors" (MILv). An ellipsoid was used as 3D distribution function for the visualization and interpretation of the MILv spatial distribution. A multivariable linear least square fitting technique was used to fit the ellipsoid function to the MILv data. Finally, a MIL tensor (or anisotropy tensor) based on the ellipsoidal coefficients was defined and calculated by means of the eigenanalysis. Eigenvalues and eigenvectors of the anisotropy tensor were used to obtain the summary numerical parameters (derivative quantities) defining orientation and anisotropy of the bread crumb. These numerical parameters are related to both anisotropy and favorite orientations of the cell walls. The anisotropy tensor eigenanalysis developed by Harringan and Mann (1984) leads to the following primary definition of the anisotropy degree (DA):

$$DA = 1 - \frac{\text{min eigenvalue}}{\text{max eigenvalue}}$$

A value of 0 corresponds to the total isotropy, whereas a value of 1 indicates the total anisotropy.

For some foods having a cellular structure, such as foamed chocolate bar, honeycomb chocolate bar, chocolate muffin, marshmallow, and strawberry mousse (Lim and Barigou, 2004) and for bread crumb (Falcone *et al.*, 2004b), the degree of anisotropy was directly determined from the 3D images. Results show that cellular food products have a concave cellular structure and a good degree of isotropy, whereas bread crumb has highly connected cells and preferential orientations of cell walls that demonstrate the orthotropic nature of this food product. Falcone *et al.* (2004b) proved that even if dissimilarities in the bread crumb macrostructure cannot be evident to naked eye, the microarchitecture has a crucial effect on the global

mechanical behavior. In fact, two samples obtained from the same slice of a bread loaf showed different shapes of the stress–strain curve.

Falcone *et al.* (2004b) determined the structural descriptors applying an algorithm able to scan the 3D digital arrays by means of a 3D version of the directed secant method (Saltykov, 1958). They extracted parameters, such as local density (or porosity), anisotropy degree, and favorite orientation of the cell walls, from a 3D tomographic image. This approach is the adaptation of the "parallel plate model" proposed by Harringan and Mann (1984) for other porous materials. According to this model, the solid phase is made of cell walls that interconnect pores; the cell walls have parallel sides (some of them are open and others are closed) and the solid phase is unevenly distributed in both the faces and edges. The algorithm used includes the following six routines.

a. 1° routine—definition of the testing volume and of the unbiased test probe. Numerical procedure begins with a specification of the size of the image array and the center coordinate of the sampling domain, a testing sphere within digital data. Next, a set of points is defined on the equatorial plane of the testing sphere so that they generate a 3D array of isotropically spaced parallel test lines (in the following called 3D lineal probe or 3D test grid). A straight line (ω_i) normal to the equatorial plane defines the sampling direction within the digital volume. Each 3D image is scanned by rotating the 3D linear probe in a lot of randomly prescribed sampling directions (ω_i). The hemispherical orientations ω_i in the coordinate system with axes k_1, k_2, and k_3 are defined by the polar coordinate (θ, φ) or by the directional cosines (x, y, z). Using polar coordinates, the colatitude θ is the angle between ω_i-direction and k_3-axis and the longitude φ is the angle anticlockwise measured between the i-axis and the projection of the ω_i-direction onto the k_1–k_2 plane.

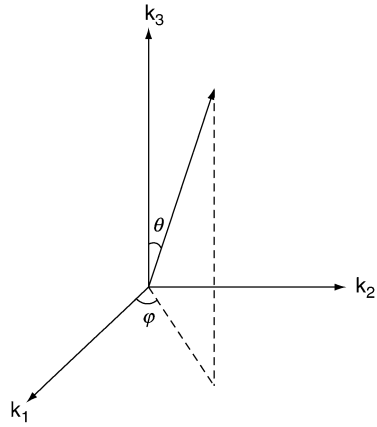

b. 2° routine-image segmentation. Based on the threshold value, the image is converted into a binary format and two basic quantities, that is, the number of voxels enclosed in the solid phase (having gray values smaller than the threshold value) and the number of voxels enclosed in the void phase (having gray values higher than the threshold one) were counted. Then the solid volume fraction δ (or density) was computed with the following formula:

$$\delta = \frac{S_v}{T_v}$$

where S_v is the number of voxels corresponding to the crumb within the testing sphere and T_v is the total number of voxels within the same volume. Porosity P (or void volume fraction) is derived as $P = 1 - \delta$.

Porosity or density are used as global structural descriptors.

c. 3° routine-voxel identification and intercept length measurement. By setting the starting position of a line segment on the boundary of the sampling domain, each test line within the testing sphere is systematically and incrementally scanned until the end point on the boundary is reached in order to determine the voxel position and the solid or void phase classification as a function of the prescribed sampling directions (ω_i). A ''two-voxels method''-based subroutine is performed as a voxel identification procedure according to Simmons and Hipp (1997). Once the scan is complete, three basic directionally dependent quantities are computed. They include $\mathbf{N(\omega_i)}$ (the number of intercept lengths), $\mathbf{\Sigma I(\omega_i)}$ (the sum of intercept lengths arising from the intersection of the test lines and the phase of interest), and $\mathbf{L(\omega_i)}$ (the length of test lines intersecting the sampling volume). Since the sampling domain has a spherical volume, $\mathbf{L(\omega_i)}$ is constant for all the sampling directions and is computed as twice the sum of all the perpendicular distances from the equatorial plane to the edge of the 3D testing sphere. $\mathbf{N(\omega_i)}$ is an *orientation-dependent* parameter recorded along a test line when the binary value of the current voxel differs from the binary value of the previous voxel. In this stereological procedure ''intercept length'' was defined as an isolate line segment arising from the intersection of a line test with the boundary of the phase of interest (solid or void) and lying in this phase. The automatic storage process and intercept identification is run for all test lines under a given number of sampling directions ($\omega_I = 128$).

Based on these three basic quantities, the mean intercept length vector $\mathbf{MIL(\omega_i)}$ is defined as an anisotropy descriptor according to Harringan and Mann (1984). This parameter indicates the dispersion of the intercept length around the sampling direction ω_I and is conceptually defined as the total line length divided by the number of intersections along the ω_i direction:

$$MIL(\omega_i) = \frac{L(\omega_i)}{N(\omega_i)}$$

Generally, **MIL(ω_i)** can be related to the solid phase as well as to the void phase according to Whitehouse (1974):

$$MIL_p(\theta, \varphi) = V_v(\omega_i) \times 2 \times MIL(\omega_i)$$

where p is the phase of interest, solid (s) or void (v), and $V_v(\omega_i)$ is the lineal fraction of p in the direction ω_i. The reason for the factor 2 is that $[2 \times MIL]$ is the mean length of a solid + void intercept.

In the numerical procedure proposed by Falcone *et al.* (2004b), the mean intercept length is related to the solid phase and $MIL_s(\omega_i)$ and is expressed in polar coordinate as the following:

$$MIL_s(\theta, \varphi) = \delta(\omega_i) \times 2 \times MIL(\omega_i)$$

where $\delta(\omega_i)$ is the lineal fraction of the solid phase in the sampling direction ω_i.

Another way to calculate the solid-related **MIL(ω_i)** vectors is the following:

$$MIL_s(\theta, \varphi) = 2^*[1 - P(\omega_i)] \times \frac{L(\omega_i)}{N(\omega_i)}$$

where $P(\omega_i)$ is the lineal fraction of the void phase in the sampling direction ω_i. Mean intercept length in the solid phase gives information about the distances between solid-void interfaces and the width of the cell walls as a function of the orientation and therefore of the 3D anisotropy. Since the $P(\omega_i)$ is an orientation-independent quantity, the effect of the anisotropy is only contained in the second term. The presence of $P(\omega_i)$ in the above-mentioned formula takes into account the fact that the mechanical properties of foamed materials apart from cellular anisotropy are strictly dependent on their porosity.

d. 4° routine—3D fitting of the MIL data distribution. The next step in the anisotropy analysis is the mathematical characterization of the directional data distribution, that is, the solid-related **MIL(θ, φ)** vectors in the 3D space. This method is based on the 2D method of Whitehouse (1974) and Harringan and Mann (1984). It consists of the plot of the positions of the end points of the MIL vectors issuing from a common centre as a function of their spherical angles. In the 3D space, this creates a pincushion-like effect with lines going in all the directions at different lengths. The distribution function that better describes the 3D shape of the directional MIL data is represented by the equation of an ellipsoid:

$$A \cdot n_1^2 + B \cdot n_2^2 + C \cdot n_3^2 + D \cdot n_1 \cdot n_2 + E \cdot n_1 \cdot n_3 + F \cdot n_2 \cdot n_3 = \frac{1}{\mathrm{MIL}^2}$$

where MIL is the magnitude of the **MIL**(θ, φ) vectors; n_i are the direction cosines between **MIL(θ, φ)** vectors and the base vectors in an arbitrary coordinate system with k_1, k_2, and k_3 axis; $A \ldots F$ are the ellipsoid coefficients. For the purpose of fitting the ellipsoid equation to the MIL data, a multivariable linear least square fitting technique is performed by solving the following linear system:

$$A_{\omega_i} \cdot \vec{x}(6) = \vec{b}_{\omega_i}$$

where A is the matrix containing the six projection data n_i, that is, the direction cosines (x, y, z), of the solid-related directional MIL(θ, φ) data for each orientation ω_I; $\vec{x}(6)$ is the six-order column vector for the corresponding six ellipsoid coefficients and $\vec{b}$ is the column vector of $1/\mathrm{MIL}^2$.

For each sampling direction ω_i, the projection data x, y, and z of each MIL(θ, φ) vector are calculated by means of the following formulas:

$$\omega_i \begin{cases} x = \sin(\theta) \times \cos(\varphi) \\ y = \sin(\theta) \times \sin(\varphi) \\ z = \cos(\varphi) \end{cases}$$

then A matrix is defined as the following:

$$\begin{aligned} A_{\omega_i}(1) &= x \cdot x \\ A_{\omega_i}(2) &= y \cdot y \\ A_{\omega_i}(3) &= z \cdot z \\ A_{\omega_i}(4) &= x \cdot y \\ A_{\omega_i}(5) &= y \cdot z \\ A_{\omega_i}(6) &= x \cdot z \end{aligned}$$

and finally, $\vec{b}$ is calculated as the following:

$$b_{\omega_i} = \frac{1}{[MIL(\omega_i) \cdot MIL(\omega_i)]}$$

The solution is:

$$\vec{x}(6) = (At \times A)^{-1} \times At \times \vec{b}$$

where At is the transpose matrix of the A matrix and $\vec{x}(6)$ provides the six ellipsoid coefficients as external variables:

$$\vec{x}(1) = A$$
$$\vec{x}(2) = B$$
$$\vec{x}(3) = C$$
$$\vec{x}(4) = D$$
$$\vec{x}(5) = E$$
$$\vec{x}(6) = F$$

The goodness of the fit is evaluated on the base of the sum of the squares of the residuals and the correlation coefficient. A great number of randomly sampled orientations were required to obtain a set of fabric descriptors that could be subjected to the application of a least squares fitting procedure. In particular, Falcone *et al.* (2004b) worked by setting 200 μ as $\tau\eta\varepsilon$ test line spacing and 128 random sampling directions for the 3D test grid so that $0 \leq \varphi \leq 2\pi$ and $0 \leq \sin(\theta) \leq 1$.

e. 5° routine-anisotropy tensor eigenanalysis. The MIL ellipsoid is related to the average distribution of the samples in the space. This ellipsoid is characterized by three axes, which are orthogonal at right angles to each other. These axes, named prinMIL$_1$, prinMIL$_2$, and prinMIL$_3$, respectively, describe the longest orientation and the length and width (major and minor axes) of the ellipse section at right angles to the longest orientation. When the test lines are oriented along the principal favorite orientation of the cell walls, the magnitude of the MIL is maximum. When the test lines are perpendicularly oriented to this direction, the magnitude of the MIL is minimum. The algorithm performs the descriptive statistics for the MIL vectors by computing the mean MIL value and the standard deviation and the descriptive statistics for the ellipsoid coefficients by computing the goodness of fit.

Several numerical parameters defining the orientation and the anisotropy degree of the directional *MIL* distribution can be computed by solving a second-rank tensor according to Harringan and Mann (1984). The second-rank tensor is usually named "fabric tensor" since it gives information about the structural symmetry and the orientation of the fabric structure. In particular, by assuming the material orthotropy, the above ellipsoid equation can be equivalently obtained as the inner product of a second-rank tensor A_{ij} with two vectors x_i and x_j as the following:

$$x_i \cdot A_{ij} \cdot x_j = 1$$

or

$$\{x_1 x_2 x_3\} \cdot \begin{Bmatrix} A_{11} & A_{12} & A_{13} \\ A_{21} & A_{22} & A_{23} \\ A_{31} & A_{32} & A_{33} \end{Bmatrix} \cdot \begin{Bmatrix} x_1 \\ x_2 \\ x_3 \end{Bmatrix} = 1$$

where the A coefficients derive from the ellipsoid fit and define the MIL tensor and x_i are the direction cosines of the mean intercept lengths in the base coordinate system with axes k_1, k_2, and k_3. In particular, the MIL tensor is defined as the following:

$$A_{ij} = \begin{vmatrix} A & D/2 & C/2 \\ D/2 & B & F/2 \\ E/2 & F/2 & C \end{vmatrix}$$

The eigenanalysis of the MIL tensor is run via Jacobi method to calculate the main characteristics values, that is, *eigenvalues* ($\hat{e}_{0-8}$), and characteristic directions, that is, *eigenvectors* ($\vec{e}_{0-8}$).

The three main eigenvectors are associated with the main orientation of the MIL ellipsoid axes, giving information about the favorite directions of the porous structure in the space. On the other hand, the three major eigenvalues are functions of the amount of solid phase (oriented intercept lengths) along each of three main eigenvectors. As a consequence, the eigenvalues are related to the anisotropy degree, whereas the eigenvectors are related to the favorite orientation of the considered porous structure.

A common way to evaluate the anisotropy of porous structures requires that the three *principal* **MILs(θ, φ)** *vectors* are derived from the 3D distribution of the directional MILs**(θ, φ)** *data*. The inverse of the square root of the absolute value of the three main eigenvalues (A, B, and C) is defined as the magnitude of the *principal* **MIL(θ, φ)** *vectors* and supplies information about the dispersion degree of the solid phase around the *principal* **MIL(θ, φ)** *vectors*.

A single fabric measure is not sufficient for the distinction of the anisotropy classes. As a consequence, several asymmetry measures are evaluated by algebrically combining the normalized eigenvalues ($\hat{\tau}_i = \hat{e}_i / \Sigma(\hat{e}_i), \hat{\tau}_1 + \hat{\tau}_2 + \hat{\tau}_3 = 1$) or the principal MILs values.

An immediate visual interpretation of the symmetry degree via the relative magnitudes of the normalized eigenvalues may be provided through the geometric visualization of the MIL tensor (Westin *et al.*, 1999), since a second-order tensor may be represented as a composite object, which is a combination of fabric shapes such as a line, disk, and sphere. The line segment describes the major principal direction of the tensor and its length is proportional to the largest eigenvalue ($\hat{\tau}_1$). The disk describes the plane spanned by the eigenvectors that corresponds to the two largest eigenvalues ($\hat{\tau}_1$ and $\hat{\tau}_2$).

The sphere has the radius proportional to the smallest eigenvalue ($\hat{\tau}_3$). In the following is shown the above mentioned scheme:

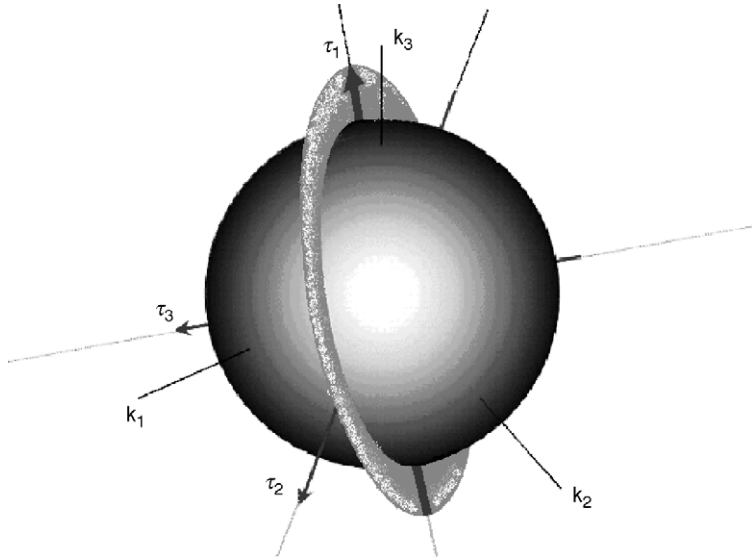

Here, the three component objects are plotted as an ellipsoid with semi-axes scaled to a maximum of 1. Thus, the length of the line segment is 1, the radius of the disk is $\hat{\tau}_2/\hat{\tau}_1$, whereas the radius of the sphere is $\hat{\tau}_3/\hat{\tau}_1$ (with $|\hat{\tau}_1| \geq |\hat{\tau}_2| \geq |\hat{\tau}_3|$).

The main orientations of the porous structure are determined by calculating both the polar coordinates, colatitude (θ) and longitude (φ), for the three main eigenvector directions with respect to the chosen coordinate system with axes k_1, k_2, and k_3:

$$O_{\tau_1}\{\vartheta\} = \tan^{-1}\left[\frac{(\vec{\tau}_6)}{\sqrt{(\vec{\tau_0})^2 + (\vec{\tau_3})^2}}\right]$$

$$O_{\tau_1}\{\varphi\} = \left\{\tan^{-1}\left[\frac{(\vec{\tau}_3)}{(\vec{\tau}_0)}\right]\right\}$$

$$O_{\tau_2}\{\vartheta\} = \tan^{-1}\left[\frac{(\vec{\tau}_7)}{\sqrt{(\vec{\tau}_1)^2 + (\vec{\tau}_4)^2}}\right]$$

$$O_{\tau_2}\{\varphi\} = \left\{\tan^{-1}\left[\frac{(\vec{\tau}_4)}{(\vec{\tau}_1)}\right]\right\}$$

$$O_{\tau_3}\{\vartheta\} = \tan^{-1}\left[\frac{(\vec{\tau}_8)}{\sqrt{(\vec{\tau}_2)^2 + (\vec{\tau}_5)^2}}\right]$$

$$O_{\tau_3}\{\varphi\} = \left\{\tan^{-1}\left[\frac{(\vec{\tau}_5)}{(\vec{\tau}_2)}\right]\right\}$$

The statistical independence of the eigenvalues at a 0.05 confidence level (α) is also tested. In this way, it is possible to distinguish among *orthotropic* structure (in which all the three eigenvalues differ each other), *transverse isotropic* structure (with two eigenvalues statistically equivalent), and *isotropic* structure (where all the three eigenvalues are equivalent).

Tables I and II report the morphological indices and the anisotropy measures obtained by Falcone *et al.* (2004b), respectively, from the stereological analysis and the eigenanalysis of the MIL tensor in order to characterize the inner crumb microstructure. By using these indices, it is possible to compare with high sensitivity the spatial arrangement of the cell walls in bread samples.

Further researches on the microstructure characterization from 3D tomographic images could be used in assessing the effect of the tomography scanning

TABLE I

ALGEBRIC EXPRESSIONS OF THE MORPHOLOGICAL FEATURES OF BREAD CRUMB SAMPLES AS OBTAINED BY THE 3D STEREOLOGICAL CALCULATION

	Symbol	Unit	Equation
Morphological descriptors	P	(*)	$P = 1 - \frac{S_v}{T_v}$
	W_N	mm^{-1}	$\frac{N(\omega_i)}{L}$
	W_Th	mm	$\delta \times \frac{L}{N(\omega_i)}$
	W_Sp	mm	$1 - \delta \times \frac{N(\omega_i)}{L}$
	SS	mm^2/mm^3	$\frac{2}{\delta} \times \frac{N(\omega_i)}{L}$

(*) nondimensional parameter.

TABLE II
ALGEBRAIC EXPRESSIONS OF THE ANISOTROPY MEASURES OF THE MIL TENSOR

Anisotropy degrees	$\text{PrinMIL}_{1,2,3}$	(*)	$\frac{1}{\sqrt{\lvert\hat{\tau}_i\rvert}}$
	Is_Ix	(*)	$\frac{\hat{\tau}_3}{\hat{\tau}_1}$
	El_Ix	(*)	$1-\frac{\hat{\tau}_2}{\hat{\tau}_1}$
	DA	(*)	$\frac{\hat{\tau}_1}{\hat{\tau}_3}$
	DA1	(*)	$\frac{\text{prinMIL}_1 - \text{prinMIL}_\text{m}}{\text{prinMIL}_\text{m}}$
	DA2	(*)	$\frac{\text{prinMIL}_2 - \text{prinMIL}_\text{m}}{\text{prinMIL}_\text{m}}$
	DA3	(*)	$\frac{\text{prinMIL}_3 - \text{prinMIL}_\text{m}}{\text{prinMIL}_\text{m}}$
	FA	(*)	$\sqrt{\frac{3}{2}}\cdot\frac{\sqrt{(\hat{\tau}_1-\hat{\tau}_m)^2+(\hat{\tau}_2-\tau_m)^2+(\hat{\tau}_3-\hat{\tau}_m)^2}}{\sqrt{\hat{\tau}_1^2+\hat{\tau}_2^2+\hat{\tau}_3^2}}$

resolution and the voxel size reconstructing resolution on the accuracy of the stereological measurements in foamed, sponge-like, and composite foods. A long-term perspective of the stereological analysis in food evaluation is the large-scale finite element analysis of the reconstructed 3D microstructure in order to evaluate or predict the material mechanical behavior.

5. *Index of connectivity*

Connectivity may be defined as the maximal number of particles (branches, cell walls, and so on) that may be cut without separating the structure. For several porous foods, such as foamed chocolate bar, honeycomb chocolate bar, chocolate muffin, marshmallow, and strawberry mousse, air cell connectivity was defined as a measure of the relative convexity or concavity of the total slid surface (Lim and Barigou, 2004). Concavity indicates connectivity, whereas convexity indicates isolated disconnected structures. Through the image analysis, authors compare the solid area and perimeter before and after an image dilation operation and calculate the index of connectivity as the following:

$$\text{Connectivity} = \frac{P_1 - P_2}{A_1 - A_2}$$

where P and A are solid area and perimeter, respectively, and subscripts 1 and 2 refer, respectively, to values measured before and after image dilation operation. Where solid connectedness results in enclosed air cell spaces, the dilation of solid surfaces will contract the perimeter. By contrast, open ends will have their perimeters expanded by surface dilation. As a consequence, a low index of connectivity indicates better-connected solid lattices, whereas a high value indicates a more disconnected solid structure. A concave structure will have a negative connectivity value, whereas a convex structure will have a positive index value.

Another method, applied to evaluate the connectivity of two-phase materials, is based on the Euler–Poincaré formula that establishes for a single solid, independently on its complexity, the following rule:

$$0.5 \times (V - E + F) + G = 1$$

where V, E, F, and G are, respectively, the number of the vertices, edges, faces, and genus that compose the surface mesh of that single solid (De Oliveira *et al.*, 2003). The genus represents the number of the handles present at the solid. In the Poincaré formula, the term $0.5 \times (V - E + F)$ is called Euler–Poincaré (EP) number that represents the key of all the determination of connectivity. This parameter is related to the connectivity and number of the connected components (particles, cells, and so on), furthermore, the connectivity is identical for the two phases. Connectivity is a scalar number and is not dependent on the orientation of the structure.

The Euler number may easily be calculated from the voxel-based data set of a 3D reconstruction. For example, the test object is fragmented into voxels, each of them representing a single solid itself. It is possible to compute the 3D morphological parameters of these solids by taking into account the following basic rule:

$$EP(A \cup B) = EP(A) + EP(B) - EP(A \cap B)$$

according to which the EP number of the union of the two sets is equal to the sum of their individual numbers minus the number of the intersections between these sets. The case in which a voxel is homeomorphic to the sphere, its EP number is 1 since their genus value is 0. When two voxels are put together side-by-side forming a new solid, it is necessary to subtract one face, that is, the contact face or interface. Then, the EP number of the new solid is 2–1 (2 of the two voxels and 1 of the one interface). The result is 1 that is in accordance with the EP number of the new solid (till homeomorphic to sphere, genus 0). Adding more and more voxels and subtracting the number of the interfaces, it is possible to calculate the EP number of the total solid. It is important to put in evidence that if a torus is formed, the EP number returns to 0 because the genus of a torus is 1 and the sum of the EP number with the genus value has to match 1, established by the Euler–Poincaré formula. A general consequence is that

when the number of the handles increase in a solid object, their *EP* number becomes more and more negative.

IV. SUMMARY

Sensorial and mechanical characteristics of food products are strongly affected by the food structural organization that can be studied at molecular, microscopic, and macroscopic levels.

Since the microstructure affects food sensorial properties, foods having a similar microstructure also have a similar behavior. Studies on food microstructure can be performed by means of a large variety of techniques allowing the generation of data in the form of images. With the development of more powerful tools, such as the X-ray computed tomographic scanners, both 2D and 3D digital images of the food internal structure can be readily acquired with high resolution and contrast and without any sample preparation. These images can be processed by means of the fractal and stereological analysis in order to quantify a number of structural elements. Fractal analysis allows the investigation of the fractal geometry in both 2D and 3D digital images. Stereology, instead, allows the obtainment of 3D features from 2D images. These data-processing techniques represent new promising approaches to a full characterization of complex internal structures. Such advances in food evaluation open new horizons for the development of mathematical and computational models able to individuate the interactions between product microstructure and their mechanical properties.

REFERENCES

Aguilera, J.M. 2000. Microstructure and food product engineering. *Food Technol.* **54**(11), 56–65.

Aguilera, J.M. and Stanley, D.W. 1999. "Microstructural Principles of Food Processing and Engineering", 2nd Ed. Aspen Publisher, Inc., Gaitherburg, MD.

Allan-Wojtas, P.M., Forney, C.F., Carbyn, S.E., and Nicholas, K.U.K.G. 2001. Microstructural indicators of quality-related characteristics of blueberries—an integrated approach. *Lebensm.-Wiss. u.-Technol.* **34**, 23–32.

Autio, K. and Laurikainen, T. 1997. Relationships between flour/dough microstructure and dough handling and baking properties. *Rev. Trends Food Sci. Technol.* **8**, 181–185.

Autio, K. and Salmenkallio-Marttila, M. 2001. Light microscopic investigations of cereal grains, doughs and breads. *Lebensm.-Wiss. u.-Technol.* **34**, 18–22.

Bache, I.C. and Donald, A.M. 1998. The structure of the gluten network in dough: A study using environmental scanning electron microscopy. *J. Cereal Sci.* **28**, 127–133.

Barcelon, E.G., Tojo, S., and Watanabe, K. 1999. X-ray computed tomography for internal quality evaluation of peaches. *J. Agric. Eng. Res.* **73**, 323–330.

Basaran, T.K., Demetriades, K., and McClements, D.J. 1998. Ultrasonic imaging of gravitational separation in emulsions. *Physicochem. Eng. Aspects* **136**, 169–181.

Basset, O., Buquet, B., Abouelkaram, S., Delachartre, P., and Culioli, J. 2000. Application of texture image analysis for the classification of bovine meat. *Food Chem.* **69**, 437–445.

Benedito, J., Carcel, J.A., Sanjuan, N., and Mulet, A. 2000. Use of ultrasound to assess cheddar cheese characteristics. *Ultrasonics* **38**, 727–730.

Benn, D.I. 1994. Fabric shape and the interpretation of sedimentary fabric data. *J. Sediment. Res.* **A64** (4), 910–915.

Bertram, H.C., Whittaker, A.K., Shorthose, W.R., Andersen, H.J., and Kalsson, A.H. 2004. Water characteristics in cooked beef as influenced by ageing and high-pressure treatment—an NMR micro imaging study. *Meat Sci.* **66**, 301–306.

Binning, G., Quate, C.F., and Gerber, C.H. 1986. Atomic force microscopy. *Phys. Rev. Lett.* **56**, 930–933.

Bonny, J.M., Rouille, J., Della Valle, G., Devaux, M.F., Douliez, J.P., and Renou, J.P. 2004. Dynamic magnetic resonance microscopy of flour dough fermentation. *Magn. Reson. Imaging* **22**, 395–401.

Bows, J.R., Patrick, M.L., Nott, K.P., and Hall, L.D. 2001. Three-dimensional MRI mapping of minimum temperatures achieved in microwave and conventional food processing. *Int. J. Food Sci. Technol.* **36**, 243–252.

Brecht, J.K., Shewfelt, R.T., Garner, J.C., and Tollner, E.W. 1991. Using X-ray computed tomography to nondestructively determine maturity in green tomatoes. *Hort. Science* **26**, 45–47.

Brunello, N., McGauley, S.E., and Marangoni, A. 2003. Mechanical properties of cocoa butter in relation to its crystallization behavior and microstructure. *Lebensm.-Wiss. u.-Technol.* **36**, 525–532.

Buffa, M.N., Trujillo, A.J., Pavia, M., and Guamis, B. 2001. Changes in textural, microstructural, and colour characteristics during ripening of cheeses made from raw, pasteurized or high-pressure-treated goats' milk. *Int. Dairy J.* **11**, 927–934.

Burch, S.F. and Lawrence, P.F. 1992. Recent advances in computerized X-ray tomography using real-time radiography equipment. *Brit. J. NDT* **34**, 129–133.

Busk, H., Olsen, E.V., and Brondum, J. 1999. Determination of lean meat in pig carcasses with the Autofom classification system. *Meat Sci.* **52**, 307–314.

Chanamai, R. and McClements, D.J. 1999. Ultrasonic determination of chicken composition. *J. Agri. Food Chem.* **47**(11), 4686–4692.

Chi-Fishman, G., Hicks, J.E., Cintas, H.M., Sonies, B., and Gerber, L.H. 2004. Ultrasound imaging distinguishes between normal and weak muscle. *Arch. Phys. Med. Rehabil.* **85**, 980–986.

Chow, R., Blindt, R., Kamp, A., Grocutt, P., and Chivers, R. 2004. The microscopic visualization of the sonocrystallization of ice using a novel ultrasonic cold stage. *Ultrason. Sonochem.* **11**, 245–250.

Cloetens, P., Barrett, R., Baruchel, J., Guigay, J.P., and Schlenker, M. 1996. Phase objects in synchrotron radiation hard X-ray imaging. *J. Phys. D Appl. Phys.* **29**, 133–146.

Coupland, J.N. 2004. Low intensity ultrasound. *Food Res. Int.* **37**, 537–543.

Coupland, J.N. and McClements, D.J. 2001. Droplet size determination in food emulsions: Comparison of ultrasonic and light scattering methods. *J. Food Eng.* **50**(2), 117–120.

Cowin, S.C. 1985. The relationship between the elasticity tensor and the fabric tensor. *Mech. Mater.* **4**, 137–147.

Cremer, D.R. and Kaletunç, G. 2003. Fourier transform infrared microspectroscopic study of the chemical microstructure of corn and oat flour-based extrudates. *Carbohydr. Polym.* **52**, 53–65.

Crippen, K.L., Hamann, D.D, and Young, C.T. 1989. Effects of grind size, sucrose concentration and salt concentration on peanut butter texture. *J. Texture Stud.* **20**, 29–41.

Crochon, M., Guizard, C., Steinmetz, V., and Bellon, V. 1994. Walnut sorting according to their internal quality: Primary results. International Conference on Agricultural Engineering, Aug. 29–Sept. 1, Milano **2**, 901.

de Campo, L., Yaghmur, A., Garti, N., Leser, M.E., Folmer, B., and Glatter, O. 2004. Five-component food-grade microemulsions: Structural characterization by SANS. *J. Colloid Interface Sci.* **274**, 251–267.

De Oliveira, L.F., Lopes, R.T., de Jesus, E.F.O., and Braz, D. 2003. 3D X-ray tomography to evaluate volumetric objects. *Nucl. Instrum. Methods Phys. Res.* **505**, 573–576.

DeHoff, R.T. and Rhines, F.N. 1972. "Microscopie Quantitative". Masson et Cie eds, p. 404, Paris.

Del Nobile, M.A., Martoriello, T., Mocci, G., and La Notte, E. 2003. Modeling the starch retrogradation kinetic of durum wheat bread. *J. Food Eng.* **59**(2/3), 123–128.

Denison, C., Carslon, W.D., and Ketcham, R.A. 1997. Three-dimensional quantitative textural analysis of metamorphic rocks using high-resolution computed tomography: Part I. Methods and techniques. *J. Metamorphic Geol.* **15**, 29–44.

Diener, R.G., Mitchell, J.P., and Rhoten, M.L. 1970. Using an X-ray image scan to sort. *Bruised Apples Agri. Engr.* **51**(6), 356–361.

Ding, K. and Gunasekaran, S. 1998. Three-dimensional image reconstruction procedure for food afficrostructure evaluation. *Artif. Intell. Rev.* **12**, 245–262.

Du, C.J. and Sun, D.W. 2004. Recent developments in the applications of image processing techniques for food quality evaluation. *Trends Food Sci. Technol.* **15**, 230–249.

Duvauchelle, P., Freud, N., Kaftandjian, V., and Babot, D. 2000. A computer code to simulate X-ray imaging techniques. *Nucl. Instrum. Methods Phys. Res.* **170**, 245–258.

Elmehdi, H.M., Page, J.H., and Scanlon, M.G. 2003. Monitoring dough fermentation using acoustic waves. *Trans. Inst. Chem. Eng. Part C* **81**, 217–223.

Elofsson, C., Dejmek, P., Paulsson, M., and Burling, H. 1997. Atomic force microscopy studies on whey proteins. *Int. Dairy J.* **7**, 813–819.

Engelsen, S.B., Jensen, M.K., Pedersen, H.T., Nørgaard, L., and Munck, L. 2001. NMR-baking and multivariate prediction of instrumental texture parameters in bread. *J. Cereal Sci.* **33**, 59–69.

Evans, R.D. 1955. "The Atomic Nucleus". McGraw-Hill, New York, PA.

Falcone, P.M., Baiano, A., Zanini, F., Mancini, L., Tromba, G., Montanari, F., and Del Nobile, M. A. 2004a. A novel approach to the study of bread porous structure: Phase-contrast X-ray microtomography. *J. Food Sci.* **69**(1), 38–43.

Falcone, P.M., Baiano, A., Zanini, F., Mancini, L., Tromba, G., Dreossi, D., Montanari, F., Scuor, N., and Del Nobile, M.A. 2004b. Three-dimensional quantitative analysis of bread crumb by X-ray microtomography. *J. Food Sci.* (in press).

Fardet, A., Baldwin, P.M., Bertrand, D., Bouchet, B., Gallant, D.J., and Barry, J.L. 1998. Textural image analysis of pasta protein networks to determine influence of technological processes. *Cereal Chem.* **75**(5), 699–704.

Feldkamp, L.A., Davis, L.C., and Kress, I.W. 1984. Practical cone-beam algorithm. *Opt. Soc. Am.* **1**, 612–619.

Fitzgerald, R. 2000. Phase-sensitive X-ray imaging. *Phys. Today* **53**(7), 23–26.

Fortin, A., Tong, A.K.W., Robertson, W.M., Zawadski, S.M., Landry, S.J., Robinson, D.J., Liu, T., and Mockford, R.J. 2003. A novel approach to grading pork carcasses: Computer vision and ultrasound. *Meat Sci.* **63**, 451–462.

Gibson, L.J. and Ashby, M.F. 1997. "Cellular Solids: Structure and Properties", 2nd Ed. Cambridge University Press, Cambridge, UK.

Goodrum, J.W. and Elster, R.T. 1992. Machine vision for cracks detection in rotating eggs. *Trans. ASAE* **39**, 2319–2324.

Grenier, A., Lucas, T., Collewet, G., and Le Bail, A. 2003. Assessment by MRI of local porosity in dough during proving. Theoretical considerations and experimental validation using a spin-echo sequence. *Magn. Reson. Imaging* **21**, 1071–1086.

Gunasekaran, S. 1996. Computer vision technology for food quality assurance. *Trends Food Sci. Technol.* **7**, 245–256.

Gunning, A.P., Wilde, P.J., Clark, D.C., Morris, V.J., Parker, M.L., and Gunning, P.A. 1996. Atomic force microscopy of interfacial protein films. *J. Colloid Interface Sci.* **183**, 600–602.

Han, Y.J., Bowers, S.V., and Dodd, R.B. 1992. Nondestructive detection of split-pit peaches. *Trans. ASAE* **35**(6), 2063–2067.

Harringan, T.P. and Mann, R.W. 1984. Characterisation of microstructural anisotropy in orthotropic materials using a second rank tensor. *J. Mater. Sci.* **19**, 761–767.

Hermann, G.T. 1980. "Image Reconstruction from Projections", p. 316. New York, Academic Press.
Hermansson, A.M., Langton, M., and Lorén, N. 2000. New approaches to characterizing food microstructures. www.mrs.org/pubblications/bulletin, December, 30–36.
Hirakimoto, A. 2001. Microfocus X-ray computed tomography and it's industrial applications. *Anal. Sci.* **17**, 123–125.
Huong, P.V. 1996. New possibilities of Raman micro-spectroscopy. *Vibr. Spectrosc.* **11**, 17–28.
Inanc, F., Gray, J.N., Jensen, T., and Xu, J. 1998. Proceedings of the SPIE Conference on Physics of Medical Imaging. Vol. 3336, p. 830.
Inglis, D. and Pietruszczak, S. 2003. Characterization of anisotropy in porous media by means of linear intercept measurements. *Int. J. Solids Struct.* **40**, 1243–1264.
Inoue, S. 1986. "Video Microscopy". Plenum Press, New York.
Ishida, N., Takano, H., Naito, S., Isobe, S., Uemura, K., Haishi, T., Kose, K., Koizumi, M., and Kano, H. 2001. Architecture of baked breads depicted by a magnetic resonance imaging. *Magn. Reson. Imaging* **19**, 867–874.
Javanaud, C. 1998. Applications of ultrasound to food systems. *Ultrasonics* **26**, 117–123.
Jones, H.E., Lewis, R.M., Young, M.J., and Simm, G. 2004. Genetic parameters for carcass composition and muscularity in sheep measured by X-ray computer tomography, ultrasound and dissection. *Livestock Prod. Sci.* **90**, 167–179.
Kaftandjian, V., Peix, G., Babot, D., and Peyrin, F. 1996. High resolution X-ray computed tomography using a solid state linear detector. *J. X-Ray Sci. Technol.* **6**, 94–106.
Kak, A.C. and Slaney, M. 1988. "Principles of Computerized Tomographic Imaging". IEEE Press.
Kaláb, M. 1984. Artifacts in conventional scanning electron microscopy of some milk products. *Food Microstruct.* **3**(2), 95–111.
Kaláb, M., Allan-Wojtas, P., and Miller, S.S. 1995. Microscopy and other imaging technique in food structure analysis. *Trends Food Sci. Technol.* **6**(6), 177–186.
Kamman, P.W. 1970. Factors affecting the grain and texture of white bread. *Baker's Dig.* **44**(2), 34–38.
Kanatani, K. 1985. Measurement of crack distribution in a rock mass from observation of its surfaces. *Soil Found.* **25**(1), 77–83.
Kanatani, K.I. 1984. Distribution of directional data and fabric tensors. *Int. J. Eng. Sci.* **22**, 149–164.
Kerr, W.L., Kauten, R.J., McCarthy, M.J., and Reid, D.S. 1998. Monitoring the formation of ice during food freezing by magnetic resonance imaging. *Lebensm-Wiss. u.-Technol.* **31**, 215–220.
Kim, N.D., Amin, A., Wilson, D., Rouse, G., and Udpa, S. 1998. Ultrasound image texture analysis for characterizing intramuscular fat content of live beef cattle. *Ultrason. Imaging* **20**, 191–205.
Kirby, A.R., Gunning, A.P., and Morris, V.J. 1995. Atomic force microscopy in food research: A new technique comes in age. *Trends Food Sci. Technol.* **6**, 359–365.
Kokelaar, J.J., van Vliet, T., and Prins, A. 1996. Strain hardening properties and extensibility of flour and gluten doughs in relation to breadmaking performance. *J. Cereal Sci.* **24**(3), 199–214.
Kulmyrzaev, A., Cancelliere, C., and McClements, D.J. 2000. Characterization of aerated food using ultrasonic reflectance spectroscopy. *J. Food Eng.* **46**, 235–241.
Kuo, A.D. and Carter, D.R. 1991. Computational methods for analyzing the structure of cancellous bone in planar sections. *J. Orthop. Res.* **9**, 918–931.
Kuo, M.I., Anderson, M.E., and Gunasekaran, S. 2003. Determining effects of freezing on pasta filata and non-pasta filata mozzarella cheeses by nuclear magnetic resonance imaging. *J. Dairy Sci.* **86**, 2525–2536.
Langton, M., Aström, A., and Hermansson, A. 1996. Texture as a reflection of microstructure. *Food Qual. Pref.* **7**(3/4), 185–191.
Leemans, V., Magein, H., and Destain, M.F. 1998. Defects segmentation on "Golden Delicious" apples by using colour machine vision. *Comput. Electron. Agri.* **20**, 117–130.
Lenker, D.H. and Adrian, P.A. 1971. Use of X-ray for selecting mature lettuce heads. *Trans. Amer. Soc. Agr. Eng.* **84**, 491–500.

Li, J, Tan, J., and Shatadal, P. 2001. Classification of tough and tender beef by image texture analysis. *Meat Sci.* **57**, 341–346.

Lim, K.S. and Barigou, M. 2004. X-ray micro-tomography of cellular food products. *Food Res. Int.* **37**, 1001–1012.

Liu, Z., Chuah, C.S.L., and Scanlon, M.G. 2003. Compressive elastic modulus and its relationship to the structure of a hydrated starch foam. *Acta Materialia* **51**, 365–371.

Maire, E., Fazekas, A., Salvo, L., Dendievel, R., Youssef, S., Cloetens, P., and Letang, J.M. 2003. X-ray tomography applied to the characterization of cellular materials. Related finite element modeling problems. *Components Sci. Technol.* **63**, 2431–2443.

Martens, H.J. and Thybo, A.K. 2000. An integrated microstructural, sensory and instrumental approach to describe potato texture. *Lebensm.-Wiss. u.-Technol.* **33**, 471–482.

Martinez, O., Salmerón, J., Guillén, M.D., and Casas, C. 2004. Texture profile analysis of meat products treated with commercial liquid smoke flavourings. *Food Control* **15**, 457–461.

Martinez, I., Aursand, M., Erikson, U., Singstad, T.E., Veliyulin, E., and van der Zwaag, C. 2003. Destructive and non-destructive analytical techniques for authentication and composition analyses of foodstuffs. *Trends Food Sci. Technol.* **14**, 489–498.

Matusani, Y., Aoky, S., Abe, O., Hayashy, N., and Otomo, K. 2003. MR diffusion tensor imaging: Recent advance and new techniques for diffusion tensor visualization. *Eur. J. Radiol.* **46**, 53–66.

McCarthy, M.J. and McCarthy, K.L. 1996. Applications of magnetic resonance imaging to food research. *Magn. Reson. Imaging* **14**, 799–802.

McClements, D.J. 1995. Advances in the application of ultrasound in food analysis and processing. *Trends Food Sci. Technol.* **6**, 293–299.

McClements, D.J. and Povey, M.J.W. 1988. Comparison of pulsed NMR and ultrasonic velocity measurements for determining solid fat contents. *Int. J. Food Sci. Technol.* **23**, 159–170.

Miquel, M.E., Carli, S., Couzens, P.J., Wille, H.J., and Hall, L.D. 2001. Kinetics of the migration of lipids in composite chocolate measured by magnetic resonance imaging. *Food Res. Int.* **34**, 773–781.

Morris, V.J. 2004. Probing molecular interactions in foods. *Trends Food Sci. Technol.* **15**, 291–297.

Morris, V.J., Kirby, A.J., and Gunning, A.P. 1999. "Atomic Force Microscopy for Biologists". Imperial College Press, London.

Novaro, P., Colucci, F., Venora, G., and D'Egidio, M.G. 2001. Image analysis of whole grains: A non-invasive method to predict semolina yield in durum wheat. *Cereal Chem.* **78**(3), 217–221.

Odgaard, A. 1997. Three-dimensional methods for quantification of cancellous bone architecture. *Bone* **20**, 315–328.

Odgaard, A., Kabel, J., Rietbergen, B., Dalstra, M., and Huiskes, R. 1997. Fabric and elastic principal directions of cancellous bone are closely related. *J. Geomech.* **30**, 487–495.

Ozutsumi, K., Nade, T., Watanabe, H., Tsujimoto, K., Aoki, Y., and Aso, H. 1996. Non-destructive, ultrasonic evaluation of meat quality in live Japanese black steers from coloured images produced by a new ultrasonic scanner. *Meat Sci.* **43**, 61–69.

Patel, D., Davies, E.R., and Hannah, I. 1996. The use of convolution operators for detecting contaminants in food images. *Pattern Recognit.* **29**(6), 1019–1029.

Peyrin, F., Salome-Pateyron, M., Cloetens, P., Laval-Jeantet, A.M., Ritman, E., and Ruegsegger, P. 1998. Micro-CT examinations of trabecular bone samples at different resolutions: 14, 7 and 2 micron level. *Technol. Health Care* **6**, 391–401.

Peyrin, F., Salome-Pateyron, M., Nuzzo, S., Cloetens, P., Laval-Jeantet, A.M., and Baruchel, J. 2000. Perspectives in three-dimensional analysis of bone samples using synchrotron radiation micro-tomography. *Cell. Mol. Biol.* **46**(6), 1089–1102.

Pietruszczak, S. and Mroz, Z. 2001. On failure criteria for anisotropic cohesive-frictional materials. *Int. J. Numer. Anal. Methods Geomech.* **25**, 509–524.

Pietruszczak, S., Inglis, D., and Pande, G.N. 1999. A fabric-dependent fracture criterion for bone. *J. Biomech.* **32**, 1071–1079.

Piot, O., Autran, J.C., and Manfait, M. 2000. Spatial distribution of protein and phenolic constituents in wheat grain as probed by confocal raman microspectroscopy. *J. Cereal Sci.* **32**, 57–71.

Povey, M.J.W. 1997. "Ultrasonic Techniques for Fluids Characterization". Academic Press, San Diego.

Povey, M.J.W. and McClements, D.J. 1988. Ultrasonic in food engineering: Part I. Introduction and experimental methods. *J. Food Eng.* **8**, 217–245.

Quevedo, R., López, G.C., Aguilera, J.M., and Cadoche, L. 2002. Description of food surface and microstructural changes using fractal image texture analysis. *J. Food Eng.* **53**, 361–371.

Rao, A.R., Ramesh, N., Wu, F.Y., Mandville, J.R., and Kerstens, P.J.M. 1992. Algorithms for a fast confocal optical inspection system. *In* "Proceedings of the IEEE Workshop on Applications of Computer Vision", pp. 298–305.

Renou, J.P., Foucat, L., and Bonny, J.M. 2003. Magnetic resonance imaging studies of water interactions in meat. *Food Chem.* **82**, 35–39.

Ridout, M.J., Gunning, A.P., Wilson, R.H., Parker, M.L., and Morris, V.J. 2002. Using AFM to image the internal structure of starch granules. *Carbohydr. Polym.* **50**, 123–132.

Ritman, E.L., Borah, B., Dufresne, T.E., Phipps, R.J., Sacha, J.P., Jorgensen, S.M., and Turner, R.T. 2002. 3-D Synchrotron μCT allows unique insight of changes in bone quality. The American Society for Bone and Mineral Research Annual Meeting, San Antonio TX, September 20–24.

Ross, K.A., Pyrak-Nolte, L.J., and Campanella, O.H. 2004. The use of ultrasound and shear oscillatory tests to characterize the effect of mixing time on the rheological properties of dough. *Food Res. Int.* **37**, 567–577.

Ryan, T.M. and Ketcham, R.A. 2002. The three-dimensional structure of trabecular bone in the femoral head of strepsirrhine primates. *J. Hum. Evol.* **43**(1), 1–26.

Saltykov, S.A. 1958. "Stereometric Metallography", 2nd ed., p. 81. Metallurgizdat, Moscow.

Sarig, Y., Gayer, A., Briteman, B., Israeli, E., and Bendel, P. 1992. Nondestructive seed detection in citrus fruits. 7th International Citrus Congress, Acireale, Italy, International Society of Citriculture **3**, 1036–1039.

Scanlon, M.G. and Liu, Z.Q. 2003. Predicting the functional properties of bread crumb from its structure. *In* "Proceedings of the 4th AOCS Annual Meeting & Expo", May 4–7, 2003, Kansas City, Kansas, USA.

Schatzki, T.F. and Fine, T.A. 1988. Analysis of radiograms of wheat kernels for quality control. *Cereal Chem.* **65**, 233–239.

Severini, C., Baiano, A., Del Nobile, M.A., Mocci, G., and De Pilli, T. 2004. Effects of blanching on firmness of sliced potatoes. *Ital. J. Food Sci.* **16**(1), 31–34.

Simmons, C.A. and Hipp, J.A. 1997. Method-based differences in the automated analysis of three-dimensional morphology of trabecular bone. *J. Bone Miner. Res.* **12**(6), 942–947.

Snigerev, A., Snigireva, I., Kohn, V., Kuznetsov, S., and Schelokov, I. 1995. On the possibilities of X-ray phase-contrast microimaging by coherent high-energy synchrotron radiation. *Rev. Sci. Instrum.* **66**, 5486–5492.

So, J.D. and Wheaton, F.W. 1996. Computer vision applied to detection of oyster hinge lines. *Trans. ASAE* **39**, 1557–1566.

Sonego, L., Ben-Arie, R., Raynal, J., and Pech, J.C. 1994. Biochemical and physical evaluation of textural characteristics of nectarines exhibiting woolly breakdown. *Postharv. Biol. Technol.* (Amsterdam) **54**, 58–62.

Stanley, D.W. 1987. Food texture and microstructure. *In* "Food Texture" (H.R. Moskowitz, ed.). Marcel Dekker, Inc., New York.

Stokes, D.J. and Donald, M. 2000. *In situ* mechanical testing of dry and hydrated breadcrumb in the environmental scanning electron microscope (ESEM). *J. Mater. Sci.* **35**, 599–607.

Sun, D.W. and Brosnam, T. 2003. Pizza quality evaluation using computer vision—part 1—pizza base and sauce spread. *J. Food Eng.* **57**, 81–89.

Suzuki, K., Tajima, T., Takano, S., Asano, T., and Hasegawa, T. 1994. Nondestructive methods for identifying injury to vapor heat-treated papaya. *J. Food Sci.* **59**(4), 855–857, 875.

Takano, H., Ishida, N., Koizumi, M., and Kano, H. 2002. Imaging of the fermentation process of bread dough and the grain structure of baked breads by magnetic resonance imaging. *J. Food Sci.* **67**(1), 244–250.

Tao, Y., Heinemann, P.H., Vargheses, Z., Morrow, C.T., and Sommer, H.I. 1995. Machine vision for color inspection of potatoes and apples. *Trans. ASAE* **38**, 1555–1561.

Thorvaldsson, K., Stading, M., Nilsson, K., Kidman, S., and Langton, M. 1999. Rheology and structure of heat-treated pasta dough: Influence of water content and heating rate. *Lebensm.-Wiss. u.-Technol.* **32**, 154–161.

Thybo, A.K., Szczypinski, P.M., Karlsson, A.H., Donstrup, S., Stodkilde-Jorgensen, H.S., and Andersen, H.J. 2004. Prediction of sensory texture quality attributes of cooked potatoes by NMR-imaging (MRI) of row potatoes in combination with different image analysis methods. *J. Food Eng.* **61**, 91–100.

Thygesen, L.G., Løkke, M.M., Micklander, E., and Engelsen, S.B. 2003. Vibrational microspectroscopy of food. Raman vs. FT-IR. *Trends Food Sci. Technol.* **14**, 50–57.

Tollner, E.W. 1993. X-ray technology for detecting physical quality attributes in agricultural produce. *Postharv. News Infor.* **4**, N149–N155.

Tollner, E.W., Hung, Y.C., Upchurch, B.L., and Prussia, S.E. 1992. Relating X-ray absorption to density and water content in apples. *Trans. ASAE* **35**, 1921–1928.

Underwood, E. 1970. "Quantitative Stereology", pp. 25–103. Addison-Wesley Publishing Company, New York.

Utku, H. and Koksel, H. 1998. Use of statistical filters in the classification of wheats by image analysis. *J. Food Eng.* **36**, 385–394.

Van Dalen, G., Blonk, H., van Aalst, H., and Hendriks, C.L. 2003. 3D Imaging of foods using x-ray microtomography. *In* "G.I.T. Imaging & Microscopy", pp. 18–21. GIT VERLAG GmbH & Co. KG, Darmstadt, Germany, www.imaging-git.com.

Van der Burg, W.J., Aartse, J.W., van Zwol, R.A., Jalink, H., and Bino, R.J. 1994. Predicting tomato seedling morphology by X-ray analysis of seeds. *J. Am. Soc. Hortic. Sci.* **119**, 258–263.

van Duynhoven, J.P.M., van Kempen, G.M.P., van Sluis, R., Rieger, B., Weegels, P., van Vliet, L.J., and Nicolay, K. 2003. Quantitative assessment of gas cell development during the proofing of dough by magnetis resonance imaging and image analysis. *Cereal Chem.* **80**, 390–395.

Vestergaard, C., Risum, J., and Adler-Nissen, J. 2004. Quantification of salt concentrations in cured pork by computed tomography. *Meat Sci.* **68**, 107–113.

Vinegar, H.J. and Wellington, S.L. 1987. Tomographic imaging of three-phase flow experiments. *Rev. Sci. Instrum.* **58**(1), 96–107.

Wendin, K., Langton, M., Caous, L., and Hall, G. 2000. Dynamic analyses of sensory and microstructural properties of cream cheese. *Food Chem.* **71**, 363–378.

West, Y.D. 1996. Study of sample heating effects arising during laser Raman spectroscopy. *Int. J. Vibr. Spectrosc.* **1**, 5.

Westin, C.-F., Maier, S., Khidhir, B., Everett, P., Jolesz, F., and Kikinis, R. 1999. Image processing for diffusion tensor magnetic resonance imaging. *In* "Medical Image Computing and Computer-Assisted Intervention". Lecture Notes in Computer Science, pp. 441–452.

Wetzel, D.L., Srivarin, P., and Finney, J.R. 2003. Revealing protein infrared spectral detail in a heterogeneous matrix dominated by starch. *Vibr. Spectrosc.* **31**, 109–114.

Whitehouse, W.J. 1974. The quantitative morphology of anisotropic trabecular bone. *J. Microsc.* **101**(2), 153–168.

Whitworth, M.B. and Alava, J.M. 1999. The imaging and measurement of bubble in bread doughs. *In* "Bubbles in Foods" (G.M. Campbell, C. Webb, S.S. Pandiella, and K. Niranjan, eds), pp. 221–231. Eagan Press, St. Paul, MN.

Wildmoser, H., Scheiwiller, J., and Windhab, E.J. 2004. Impact of disperse microstructure on rheology and quality aspects of ice cream. *Lebensm.-Wiss. u.-Technol.* **37**, 881–891.

Wium, H., Pedersen, P.S., and Qvist, K.B. 2003. Effect of coagulation conditions on the microstructure and the large deformation properties of fat-free Feta cheese made from ultrafiltered milk. *Food Hydrocolloids* **17**, 287–296.

www.geog.ubc.ca/courses/geog470/notes/image_processing.

www.hei.org/research/depts/aemi/emt.htm.

www.nikon-instruments.jp/eng/tech/1-0-4.aspx.

www.plbio.kvl.dk/~als/confocal.htm.

www.ruf.rice.edu/~bioslabs/methods/microscopy/microscopy.html.

Xu, Y.-H. and Pitot, H.C. 2003. An improved stereologic method for three-dimensional estimation of particle size distribution from observations in two dimensions and its application. *Comput. Methods Programs Biomed.* **72**, 1–20.

Yada, R.Y., Harauz, G., Marcone, M.F., Beniac, D.R., and Ottensmeyer, F.P. 1995. Visions in the mist: The Zeitgeist of food protein imaging by electron microscopy. *Trends Food Sci. Technol.* **6**, 265–270.

Yan, Z.Y., McCarthy, M.J., Klemann, L., Otterburn, M.S., and Finley, J. 1996. NMR applications in complex food systems. *Magn. Reson. Imaging* **14**, 979–981.

Yantarasri, T., Kalayanamitra, K., Saranwong, S., and Sornsrivichai, J. 2000. Evaluation of the maturity index for durian fruit by various destructive and non-destructive techniques. Quality assurance in agricultural produce. *In* "ACIAR Proceedings" (G.I. Johnson, Le Van To, Nguyen Duy Duc, and M.C. Webb, eds), pp. 700–705.

Yantarasri, T. and Sornsrivichai, J. 1998. Internal quality evaluation of tangerines. *Acta Hortic.* **464**, 494.

Yantarasri, T., Sornsrivichai, J., and Chen, P. 1997. Nondestructive X-ray and NMR imaging for quality determination of mango fruit. Presented at the 5th International Symposium on Fruit, Nut and Vegetable Production Engineering, Davis, California.

Yantarasri, T., Sornsrivichai, J., and Kalayanamitra, K. 1999. Nondestructive techniques for quality evaluation of pineapple fruits. The Third International Pineapple Symposium, Pattaya, Thailand.

Zwiggelaar, R., Bull, C.R., Mooney, M.J., and Czarnes, S. 1997. The detection of 'soft' materials by selective energy X-ray transmission imaging and computer tomography. *J. Agric. Eng. Res.* **66**(3), 203–212.

Zwiggelaar, R., Bull, C.R., and Mooney, M.J. 1996. X-ray simulations for imaging applications in the agricultural and food industries. *J. Agric. Eng. Res.* **63**, 161–170.